Design of a miniature wind turbine with Albatrozz flaps

Sassen, Bart J.P.

Award date:
2023

Technische Universiteit
Eindhoven
University of Technology

Department of Mechanical Engineering
Master Sustainable Energy Technology
Section of Energy Technology
www.tue.nl/en/research/research-groups/energy-technology

Author
B.J.P. Sassen

Student number
1635956

Chair graduation committee
Prof.Dr.Ir. Harald van Brummelen

Responsible Lecturer TU Eindhoven
Dr.Ir. Clemens Verhoosel

Supervisor RU Groningen
Prof.Dr. Eize Stamhuis

Independent/external member
Dr.Ir. Hamid Montazeri

Credits
45 EC

Date
July 14, 2023

Design of a miniature wind turbine with Albatrozz flaps.

Phase 2 Report of the Graduation Project : Project phase

B.J.P. Sassen
b.j.p.sassen@student.tue.nl

Student number : 1635956

This Master's thesis has been carried out in accordance with the rules of the TU/e Code of Scientific Integrity.

university of groningen

ALBATROZZ

Where innovation starts

Asbtract

In this masters thesis report a design is made for an oscillating flap on the trailing edge of a one meter diameter wind turbine. The design is used in experiments in a closed-loop wind tunnel to test the influence of dynamic stall (DS) on the aerodynamic performance of the wind turbine. DS is a complex aerodynamic phenomena that occurs on helicopters and wind turbines as well as many other aerodynamic devices. Research by McAlister et al. (1978), McCroskey (1981) and Carr (1988) has found that DS is a response to a quick unsteady change in angle of attack (AOA) beyond the steady-state stall angle and is characterised by a large dynamic stall vortex (DSV). This vortex delays the process of stall and can significantly increase the generated lift. Nevertheless, according to Mulleners and Raffel (2013) the highly unsteady unsteady aerodynamic loads during DS decreases the aerodynamic efficiency in time whilst increasing the structural forces and bending moments. However, research on dynamic stall using a bio-mimetic approach by Matz (2010), Noffke (2011), Beil (2016), Marchant (2017) and Schweickert (2016) in the bio-mimetic research group of Prof. E.J. Stamhuis at the University of Groningen has shown that a high oscillation frequency can reduce the negative effects of DS whilst maintaining the positive effects. The experimental research of Noffke (2011) using a 3D model of a Fulmar wing in a flow tank has shown that the large hysteresis curve, that is often associated with DS, can be reduced to a straight line.
Wind turbines can use dynamic stall in the partial load region to increase electrical energy generation. The partial load region is the region in which the generator is not yet at maximum capacity. This is particularly beneficial for land-based turbines, which generally operate more time in the partial load region compared to the full load region.
The research on dynamic stall in the bio-mimetic research group continued with Janssen (2018), Mahfoozi (2020) and Neven (2020) who designed and tested a small one diameter wind turbine with *LEO*-blades. *LEO*-blades refer to blades that are cut in half in span-wise direction. The outer half of the blade is able to oscillate to induce the dynamic stall. This design, however, poses a structural safety hazard when applied on large scale wind turbines. Hence this thesis focuses on the design of an oscillating flap on the trailing edge (TE) of the blade, such that the structural integrity of the blade stays intact. The blades are then connected to a small generator to be able to perform wind tunnel testing. The main goal of this project is to design the flaps and its oscillating mechanism. The research question that should be answered by the results of the experiments is: "What is the influence of the frequency and the amplitude of the oscillation on the aerodynamic efficiency of the rotor due to the influence of dynamic stall".
The extended *Euler-Bernoulli beam theory* for large deflections is used to design a bending TE flap. The bending of this flap is driven by an oscillating rod connected to a toy helicopter tail rotor.
During the design process, another question arose: "What is the influence on the flap length in chord-wise direction on the aerodynamic efficiency of the dynamic stall phenomenon". To answer this question, some CFD analyses are performed in which two different flap lengths are compared. First some steady-state analyses are performed to refine the mesh, after which some dynamic analyses are performed to analyse the influence of the flap length as well as the frequency and amplitude on the resulting lift. The results of the CFD analyses show that if the induced change in AOA is equal for both the shorter and larger flap, then a shorter flap has the largest increase in generated lift. This is due to a larger vertical component of the velocity field at the TE for a smaller flap. The analyses also show that a larger amplitude directly increases the generated lift and a higher oscillation frequency reduces the hysteresis effect.
The wind tunnel tests show that the flap design works as intended. The flap is able to oscillate at relatively high frequencies of about 15 [Hz]. The frequency is limited by the power of the stepper motor. The original setup did not allow to accurately test the influence of dynamic stall on the aerodynamic performance of the turbine. This is because the generator was too small for the aerodynamic power, which resulted in a too high rotational speed and very low angles of attack ranging from zero to eight degrees depending on the free-stream velocity and the span-wise location. To accurately test dynamic stall, the angles of attack should be about eight degrees. The original generator was replaced with a

stronger sensored generator which allowed for more controlled rotational speeds. Unfortunately, due to time constraints it was not yet possible to test the influence of the oscillation frequency on dynamic stall.

Symbols

Symbol	Description	SI unit
α	Angle of attack	[°]
Θ	Twist angle	[°]
$\Theta_{polynomial}$	Polynomial describing the twist distribution	[°]
κ	Reduced frequency	[−]
λ	Tip-speed-ratio	[−]
λ_r	Speed-ratio tangential velocity vs free-stream wind	[−]
ρ	Density	[kg/m^3]
$\rho(x_i)$	Curvature in point x$_i$	[m^{-1}]
$\rho_{original}$	Original curvature	[m^{-1}]
Φ	Inflow angle	[°]
Ω	Rotational speed	[rad/s]
$\Omega(RPM)$	Rotational speed	[RPM]
A	Reference area	[m^2]
B	Number of blades	[−]
$b(x_i)$	Thickness in point x$_i$	[m]
c	Chord length	[m]
C_d	Drag coefficient	[−]
C_l	Lift coefficient	[−]
C_{opt}	Optimum chord length	[m]
$c_p(s)$	Pressure coefficient at mesh vertex *s*	[−]
$C_{polynomial}$	Polynomial describing the chord length distribution	[m]
E	Young's modulus	[N/mm^2]
f	Frequency	[Hz]
F_D	Drag force	[N]
F_t	Tangential force	[N]
F_x	Force in x direction	[N]
F_y	Force in y direction	[N]
L	Lift force	[N]
h	Span-wise length of flap	[m]
I_L	Line current	[A]
I_{PH}	Phase current	[A]
$L(x_i)$	Length at coordinate x$_i$	[m]
Re	Reynolds number	[−]
r	Span-wise radius	[m]
R	Total radius	[m]
R_{new}	Radius after bending	[m]
r_{min}	Minimum radius to describe a $^1/_4$ circle with given length	[m]
$r_{original}$	Original radius	[m]
$r(x_i)$	Radius in point x$_i$	[m]
M_A	Bending moments in point A	[Nm]
	Bending moment in point Φ	[Nm]
n	Number of pole pairs	[−]
$p(s)$	Pressure at mesh vertex s	[N/m^2]
p_∞	Free-stream (static) pressure	[N/m^2]
P_{wye}	Power generated in a wye configured generator	[W]
$n_x(s)$	Normal vector in x direction at vertex *s*	[−]

Symbol	Description	SI unit
$n_y(s)$	Normal vector in y direction at vertex s	$[-]$
S	Characteristic length	$[\mathrm{m}]$
t	Time	$[\mathrm{s}]$
U_{rated}	Rated wind speed	$[\mathrm{m/s}]$
U_∞	Free-stream velocity	$[\mathrm{m/s}]$
V_L	Line voltage	$[\mathrm{V}]$
V_{PH}	Phase voltage	$[\mathrm{V}]$
V_{res}	Resultant velocity	$[\mathrm{m/s}]$

Acronyms

2D Two Dimensional

3D Three Dimensional

AOA Angle of attack

CFD Computational Fluid Dynamics

(D)PIV (Digital) Particle Image Velocimetry

DS Dynamic Stall

DSV Dynamic Stall Vortex

DU Delft University

FFA FL YGTEKNISKA FORSOKSANSTALTEN (Swedisch aviation testing institute

HP High pressure

KNMI Koninklijk Nederlands Meteorologisch Institute

LE Leading Edge

LEO Lift Enhancement due to Oscillations

LEPS Lift Enhanced Periodic Stall

LES Large Eddy Simulation

LP Low pressure

MEXICO Measurements and Experiments in Controlled Conditions

MexNext Follow-up project on the MEXICO project

NACA National Advisory Committee for Aeronautics

NREL National Renewable Energy Laboratory

PDE Partial Differential Equation

PLA Polylactic acid

RANS Reynolds-Averaged Navier-Stokes

RISØ Danish National Laboratory for Sustainable Energy

RPM Rotations per minute

SST (Menter's) Shear Stress Transport turbulence model

TE(V) Trailing Edge (Vortex)

TPU Thermoplastic Polyurethane

TSR Tip-speed ratio

TU Technical University

List of Figures

List of Tables

Technische Universiteit
Eindhoven
University of Technology

Table of contents

Title
Design of a miniature wind turbine with Albatrozz flaps.

1 Introduction

1.1 Background

During the past couple of decades climate change has become an increasingly more discussed topic. According to IPCC (2023), researchers have found indisputable proof that the human enhanced greenhouse effect does result in global warming. In addition, recent changes in global warfare has shown western civilisations a need for energy independence. As a result, there is a positive change in society's support for the transition to sustainable energy sources. To achieve this transition, a large increase in installed capacity of renewable energy sources, predominantly solar and wind, is needed.

All wind turbine models have a different rated wind speed, but most are close to or above 10 [m/s]. According to weather data from KNMI (2022) the wind speeds on land in the Netherlands at a height of 100 [m] are below 10 [m/s] for 80% of the year. As a consequence, most turbine models on land in the Netherlands waste a decent amount of potential energy conversion. The research project of Stamhuis et al. (2019) tries to tackle this problem. By studying birds they noticed that during landing when the speed of the bird decreases, smaller birds start to flap their wings to compensate for the loss of lift. However, they also noticed that larger birds, like the Albatross, are not able to do this. Instead, Albatrosses evolved an oscillatory motion of their wings to temporarily increase the AOA and as a result increase the lift force, without separating the airflow over their wings. This technique could also be used in wind turbines to increase the energy output at lower wind speeds.

According to Manwell et al. (2010a) only steady state aerodynamics are used to generate lift in modern wind turbines. Modern wind turbines transform the relatively *'linear'* motion of the wind through the plane of rotation into a tangential motion of the rotor by creating a pressure difference over the blade (Neven and Stamhuis, 2019). The aerofoils accelerate the oncoming airflow in the opposite direction of the rotation. According to Newton's 1^{st} and 3^{rd} law, this acceleration causes a counter-force, the lift force, in opposite direction to account for the impulse created by the airflow. The size of the lift force is dependent on the wind speed and the blade design. The blade consists of a few different aerofoil designs, twist angles and chord lengths as shown in Figure 1.1. These parameters are all dependent on the radius along the blade. In general thinner aerofoils have a greater lift-to-drag ratio and hence create more lift force for a given relative wind speed. The sum of the viscous and pressure force can be decomposed into two other forces: the lift and drag forces (Zaaijer and Viré, 2021). The viscous force is dependent on the wetted area and the pressure force is dependent on the frontal area. Thinner aerofoils have a smaller wetted area as well as a smaller frontal area and hence the drag force is smaller. This is important, as a smaller drag force implies that a larger portion of the pressure and viscous force is transformed into lift.

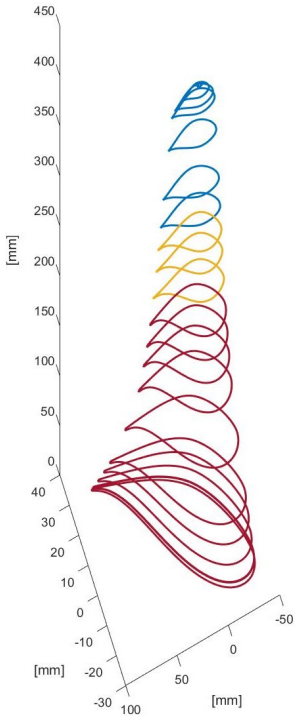

Figure 1.1: Different aerofoils creating a single blade.

The lift-to-drag ratio is a curve as function of the AOA. At lower angles of attack this curve increases relatively linear, but at higher angles the curve starts to flatten out before it drops again. After a small drop the lift curve enters the stall region, where the airflow is fully detached from the leading edge. The optimum AOA of each aerofoil is the AOA at which the lift-to-drag ratio is highest. This is not only de-

pendent on the shape of the aerofoil, but also on the Reynolds number at which the turbine operates. The Reynolds number is an important dimensionless parameter, as it relates the inertial to viscous influence on an object (Ge et al., 2015). Hence when the Reynolds number is constant it can be used to compare different aerofoils. Different Reynolds numbers directly influence the performance of a turbine rotor. If the Reynolds number changes, so should the design of the blade to ensure that the blade operates under ideal conditions.
Turbines blades are usually designed such that each aerofoil along the blade operates just below its optimum AOA. This is achieved by adding a twist to the blade such that the twist and AOA add up to the relative inflow angle, the angle of the incoming wind caused by the rotational motion of the blades. The twist angle is large at the root of the blade and decreases to zero toward the tip of the blade. The chord line of the aerofoil at the tip of the blade is designed to be in-line with the linear airflow, to reduce the vortices created at the tip of the blade. Because of this, the AOA at the tip of the blade of smaller turbines is often far below the optimum AOA, as the lower Reynolds number causes some aerofoils to increase the optimum AOA whilst the inflow angle remains the same.
The low moment of inertia due to the thin design makes thinner aerofoils susceptible to the large bending moments created by the large forces on long blades. Hence, at the root of the blade, where the blade is connected to the hub, the aerofoil is much thicker to accommodate for the higher bending moments. Toward the tip of the blade the arm of the bending moments is much shorter and hence the magnitude of the moment is much lower. Thinner aerofoils are used at the tip to maximize the lift-to-drag ratio. In between these aerofoils are transitioning aerofoils, going from thicker at the root to thinner toward the tip, to create a smooth blade. However, to further reduce the vortices created at the tip of the blade the chord length is reduced to be much lower than the optimal chord length. As stated before, the chord length also has an influence on the size of the generated lift force. This is important to realize for the project, as this implies that the bulk of the lift force is generated by the middle section of the blade rather than the tip section.

1.2 Literature review

As stated before, the AOA along the span of the blade is designed to be below the optimum AOA. This is done to account for gusts in turbulent airflow. Due to the large mass of the rotor the angular speed changes slowly whilst during a gust the wind speed changes very rapidly. This causes the inflow angle and as a result the AOA to increase. If blades were designed to have an optimal AOA gusts could drag the lift curve of the blade into the dynamic stall region. Choudhry et al. (2016) states that dynamic stall, also called *Lift Enhanced Periodic Stall* (LEPS), is a process in which the separation of the airflow is delayed due to a rapid excursion in the AOA beyond the steady-state stall angle. Due to the delay of the flow separation, whilst still increasing the AOA, the lift is increased beyond the steady-state maximum lift. In addition, a coherent vortex is created near the leading edge of the blade due to flow reversal on the blade surface. This vortex, a dynamic stall vortex, further increases the lift. As soon as the vortex sheds the airfoil goes into deep stall. At this point the airflow delaminates and the lift decreases significantly. The AOA has to be reduced in order to reattach the airflow to the blade. Figure 1.2 shows the different stages during dynamic stall and compares the lift and drag coefficients as function of the AOA during steady-state stall and unsteady (dynamic) stall. Research, including the reports by Carr et al. (1977), Corke and Thomas (2015) and McIntosh (2009), classify dynamic stall as a highly complex problem and an undesired phenomenon. This is because, once the AOA is lowered again, their research found that the lift does not follow the same curve backwards but rather a lower one. Hence a lot of lift is lost during the cycle. Figure 1.3 shows an illustration of a typical lift-coefficient curve during a dynamic stall cycle by Corke and Thomas (2015). A large hysteresis in the lift force is observed when the angles of attack are reduced after deep stall. This indicates a delay in flow reattachment and lift recovery.

The past few decades LEPS has been considered to be a negative phenomenon especially for helicopters

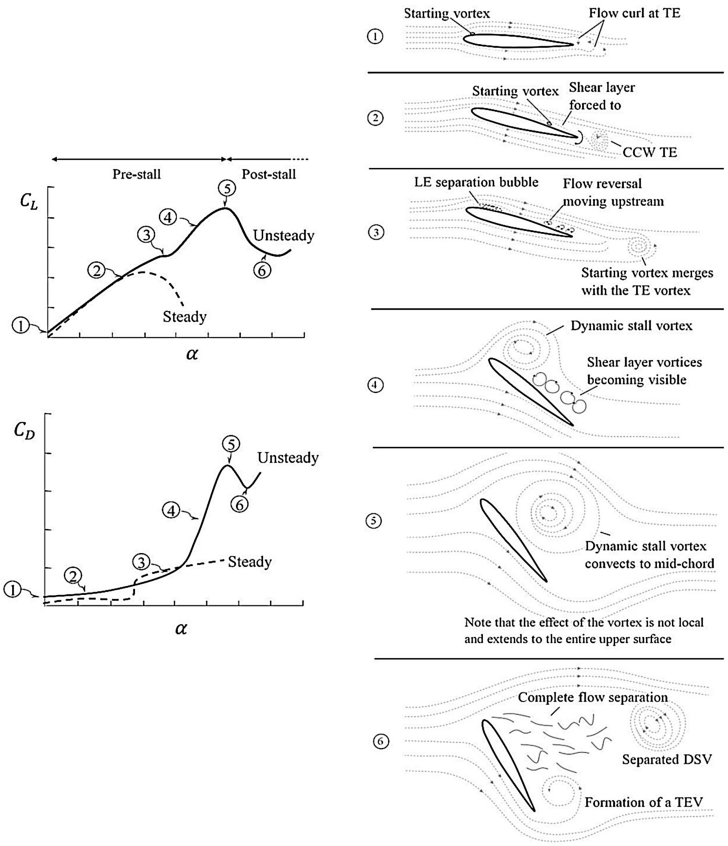

Figure 1.2: Process of dynamic stall (image reproduced fromChoudhry et al. (2016)).

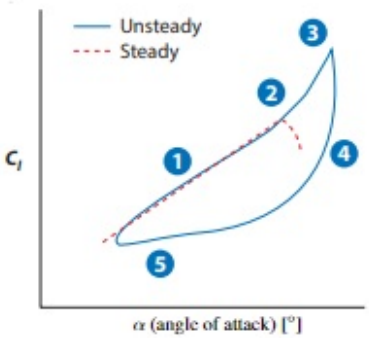

Figure 1.3: Illustration of a typical dynamic stall cycle (image reproduced from Corke and Thomas (2015)).

(a) Northern Fulmar (image reproduced from Bird Guides (2022))

(b) Wandering Albatross (image reproduced from Wallpapergeeks (2014))

Figure 1.4: Birds that perform an oscillatory motion with their wings during landing.

but also for wind turbines. However, the Albatrozz research that started in 2011 has shown that the LEPS effect can be used as an advantage toward lift generation.
During landing, birds slow down to reduce the force of impact with the surface. The slower speed causes loss of lift and as a result many birds start flapping their wings to compensate this. However, larger birds like the Wandering Albatross or the Northern Fulmar seem to behave differently. Georg Rüppell (1977) was first to describe and examine in detail that these birds use an oscillatory motion of the wing, instead of a flapping motion, to compensate for the loss of lift during landing. This is further explained by Warham (1991) who states that the oscillatory motion, called fanning, increases the aerodynamic coefficients of the wing. The Albatrozz research started with the report of Matz (2010) who performed numerical simulations on the *'fanning'* of the basic NACA0012 test profile. His simulations showed that the averaged lift on the oscillating NACA0012 profile is higher than the lift created by the same profile without oscillations. The lift enhancement adds up to about 18% in the two-dimensional case and up to about 10% in the three-dimensional case.
The research continued with the report of Noffke (2011) who performed Particle Image Velocimetry (PIV) simulations on a fulmar wing to see the effects of wing fanning on the generated lift and to confirm that Fulmars indeed use the LEPS effect during landing. As a comparison the NACA0012 aerofoil profile was also modelled using PIV. The experiments showed that the cambered profile of the Fulmar wing was not as much affected by the dynamic stall effect compared to the NACA 0012 profile, which displayed classical and pronounced dynamic stall at the utilised reduced frequencies. Especially at higher frequencies the hysteresis effect could be avoided with the Fulmar profile resulting in an increased lift production. The fastest oscillation frequency resulted in an increase of about 24% in generated lift compared to the 9^o steady-state incident case.
The report of Beil (2016) creates the first real link between the biological use of the LEPS effect, in the landing behaviour of Albatrosses and Fulmars, and the possible technical application in wind turbines. Beil (2016) used 2D Reynolds-Averaged Navier-Stokes (RANS) simulations to compute the lift and drag coefficients both for static and dynamic scenarios for three different aerofoils. The tested aerofoils include the S809 aerofoil by NREL, the DU-93-W-210 by Delft university and again the NACA 0012. In addition Beil (2016) also modelled a simple blade based on one single aerofoil, the DU-93-W-210 aerofoil, to compute and compare the power generation of the stationary case versus the different dynamic cases. Moreover, also the input energy for the pitching motion is computed. The results showed that the NACA 0012 profile under dynamic loading could reach a maximum lift coefficient along the cycle of almost 200% of the maximum static value. The DU-93-W-210 profile showed a maximum increase in lift coefficient of about 7% under dynamic loading compared to the steady-state. Unfortunately the power generation computations showed that the dynamic cases actually resulted in a loss of power generation compared to the steady-state case. Beil (2016) explains this by the fact that the drag coefficients increased even more compared to the lift coefficients. All drag coefficients for the dynamic simulations increased between 70% and 250% compared to the stationary drag coefficient at maximum lift. An important lesson to draw from this is again that the design of the aerofoil has a large influence on the net gain that can be achieved by the LEPS effect.
Schweickert (2016) continues the research by performing the first flow tank experiments with an actual wind turbine blade design. The designed LEO-blade is based on the MEXICO-blade from the MexNext project (Zhang et al. (2014), Schepers et al. (2012), Schepers et al. (2018), Boorsma and Schepers (2014)) with some adjustments. *'LEO'* stands for Lift Enhancement due to Oscillation and the main difference with a normal wind turbine blade is that the LEO-blade is divided radially into two parts. The root or base part is steady and the tip part is able to oscillate at different frequencies. The main changes to the MEXICO blade are the change of the middle aerofoil from RISØ-A1-21 to FFA W3-211 and the removal of the base cylinder at the root of the blade. Instead of the base cylinder the curve of the chord length distribution is extended to the start of the blade. The RISØ-A1-21 aerofoil was replaced by the FFA W3-211 aerofoil as the exact coordinates of the RISØ-A1-21 aerofoil were not available. During the Digital Particle Image Velocimetry (DPIV) measurements of the LEO-blade in the flow tank, the LEO-blade was oscillated around an axle located at 30% of the chord length. The experiments of

Schweickert (2016) proof that lift enhancement is possible for oscillating blades. The results show that an oscillation amplitude of 0^o to 20^o degrees increase the average lift with a factor of about 2.4 and the lift-to-drag ratio is increased with about 20%. Other amplitudes show an increase in average lift aswell, but with a decrease in lift-to-drag ratio.

The masters thesis of Marchant (2017) too performed DPIV measurements in a flow tank on the oscillating LEO-blade and found similar results as Schweickert (2016). Especially for lower flow velocities of about 0.4 [m/s] the lift-to-drag ratio at an oscillation amplitude of 0^o to 20^o resulted in an increase of 150% or 2.5 times the lift-to-drag without oscillations.

After the final flow tank tests of Marchant (2017) a step toward a real wind turbine is taken in the report of Janssen (2018). Janssen (2018) designed and build a miniature one meter diameter wind turbine using the LEO-blades and tested it in the wind tunnel of the University of Groningen. The wind turbines was tested for wind speeds ranging from 0 to 4.5 [m/s]. The results of the experiments performed by Janssen (2018) proof that lift enhancement due to oscillation of the blades works and that the power generation in the partial load region can be increased compared to non-oscillating turbines. Janssen (2018) tested three different amplitudes, of which two include negative amplitudes, and five different frequencies. The scenario with an oscillation amplitude of 0^o to 10^o showed the best results and the power output increased with increasing frequencies.

Further research into the LEO-blade wind turbine design was conducted by Mahfoozi (2020) who redesigned the turbine such that higher oscillating frequencies above 18.8 [Hz] could be achieved.

Neven (2020) improved the design of Mahfoozi (2020) by increasing the tip-speed-ratio and reducing the mechanical stress inside the turbine. Neven (2020) again tested the lift enhancement and increased power generation of the turbine by conducting different experiments on oscillating amplitude and frequency. The main findings of the experiments performed by Neven (2020) were that an oscillation amplitude of 0^o to 10^o performed best and that negative angles of attack, like -10^o to 10^o performed worst.

After the experiments of Neven (2020), the Albatrozz team wanted to implement and test the technology on a real size turbine. However, regulations prevented this as the design was considered to be too fragile. Older and smaller turbines usually have a spar in the centre which carries the load on the blade. For this design the spar has to be cut in half and hence it would be uncertain if the load could be carried by the relatively small axle which oscillates the outer half of the blade.

In the new design, instead of cutting the blade in half and oscillating the entire outer part of the blade a few smaller flaps are cut out of the trailing edge of the blade. By oscillating these flaps the shape of the aerofoil and with it the chord length and AOA are changed. This does not require the spar to be cut in half and hence is stronger. The blades are already being manufactured to be tested on a real scale turbine. This report will focus on designing the flaps on a much smaller model scale turbine, which will then be manufactured and tested in a wind tunnel. The report will begin with a design study on how the oscillatory motion can be achieved on such a small scale. Next some experiments will be conducted in the wind tunnel to show that indeed the oscillatory motion increases the energy yield at lower wind speeds and how much.

1.3 Research definition

In the following chapter the definition of the research is defined in detail. Section 1.3.1 defines the problem. In Section 1.3.2 the aim of the research is defined by focussing on the goals and sub-objectives. In Section 1.3.3 the metrics for measuring success of the project are enumerated and in Section 1.3.4 the outline of the thesis is presented. The stakeholders of this project, and their roles, can be found in appendix A.

1.3.1 Problem definition

The main problem with the blade design made during the master thesis's of Janssen (2018), Mahfoozi (2020) and Neven (2020) is that the blade oscillates around a tiny axle through the middle of the blade. For this to be implemented on a larger scale the spar of real size turbines has to be cut in half. This comes with great constructional risks. A new design, using oscillating flaps on the trailing, is currently being tested on a real size Vestas V52 wind turbine. To compare and validate the test results of the larger turbine, a smaller scale model should be designed and tested as well. The main problem with the new design is that the control system of the oscillatory motion is placed inside the blade of the turbine. The blades of the scale model are much smaller and hence the control system, how it is designed for the bigger turbine, does not fit in the scale model.

1.3.2 Research aim, project goals and objectives

The aim of this research is to design a system that can oscillate the *Albatrozz* flaps on the trailing edge of a one meter diameter scale wind turbine model and to follow-up were Neven (2020) left of. More experiments with respect to amplitudes and frequencies should be done to get a better insight into effects of different configurations of the oscillations on the increase in power generation. The results can be used after the project to compare with the data of a full scale *'Vestas V52'* wind turbine that is being retrofitted.

Main research questions :

- Can an oscillation system be designed for the flaps on the trailing edge of the blades on the scale wind turbine model?
- What is the influence of different frequency settings of the flaps on the power generation?

The main goal of the project, which is to deliver a design of a system that can oscillate the flaps on a 1[m] diameter scale wind turbine model, can be divided into a few objectives. The first objective is to get a design for bendable flaps such that the angle of attack changes depending on the shape of the bend. A second objective is to design a system which can control the bending of the flaps using repetitive motion. A third objective for this goal is to design the system such that the shape of the flaps can be held steady at the original design angle of attack. This is required to perform measurements without oscillating flaps.

1.3.3 Metrics for measuring success

This Section lists the metrics for measuring success. These metrics are important as they can quantifiably check the result of the project.

The first metric to measure the success of the project is a working 1[m] diameter scale model wind turbine with Albatrozz technology. This metric can also be divided into a few sub-metrics which are listed below.

1. Flaps are able to bend.
2. The flaps on the blades are able to oscillate freely in the wind speed range of [0-5][m/s] whilst the turbine is rotating.

The second metric to measure the success of the project is the ability of the flaps to oscillate at different pre-determined frequencies.

The third metric to measure the success of the project is the ability to measure efficiency increase or decrease of the turbine using oscillating flaps compared to the same turbine without oscillating flaps.

1.3.4 Outline of the thesis

In Chapter 1 of this thesis the background on wind turbines and the literature on dynamic stall are introduced.
Chapter 2 discusses the methods used to test the theory. The methodology chapter consists of five sections. Section 2.1 examines the blade which was designed during previous research to make sure that the blade itself is properly designed for the experimental aerodynamic conditions. Section 2.2 covers the design of the oscillating flap and its driving mechanism. Section 2.3 elaborates upon the structural integrity of the rotor. In particular the connection between the nosecone and the blades. Section 2.4 presents the experimental test setup as well as the performed tests and Section 2.5 looks into the CFD model.
Chapter 3 analyzes the results of this thesis. The results are divided into two sections. Section 3.1 looks into the results of the wind tunnel experiments and Section 3.2 addresses the results of the CFD analyses.
Chapter 5 elaborates on the final conclusions of this thesis and Chapter 4 discusses the relevance of this thesis with respect to previous studies and potential future research.

2 Methodology

In this chapter the methods used to accomplish the goals of this project are discussed. Section 2.1 discusses how the general parameters of the blade, like twist distribution, chord distribution and the used aerofoils are determined. Section 2.2 elaborates upon the design of the oscillating flap and its driving mechanism. Section 2.3 focuses on the structural strength of the turbine. In specific the connection of the blades to the nosecone. Section 2.4 presents the experimental test setup and the performed tests. Finally Section 2.5 covers the model builder of the CFD analyses.

2.1 Blade design

As stated in the introduction of this report, the biomimetic research on dynamic stall has been ongoing for a decade. In recent years the LEO-blade was designed and tested both static, in a flow tank, and dynamically in a flow tank as well as a wind tunnel. The LEO-blade is based on the design of the Mexico-blade from the Mexnext-project. Details about this project can be read in the report of Zhang et al. (2014).

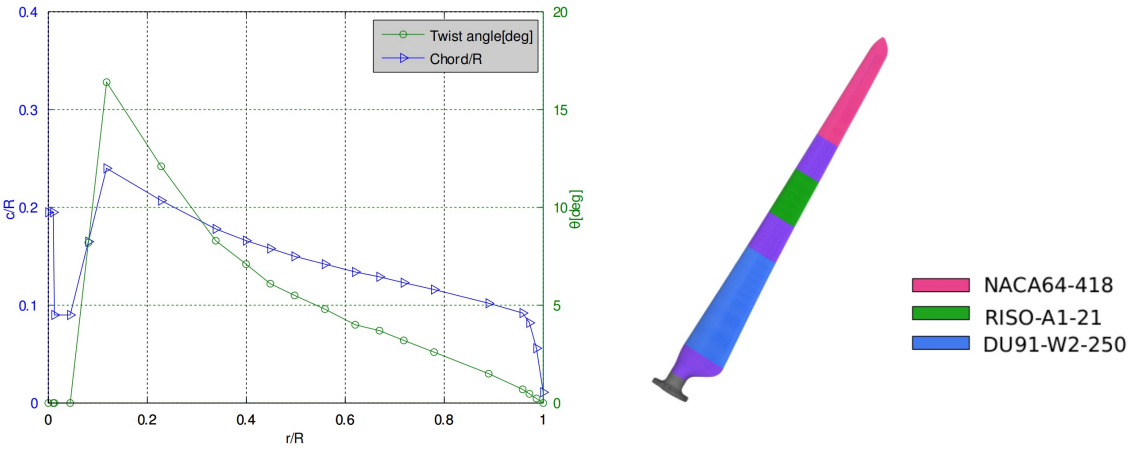

(a) Dimensionless chord and twist distribution.

(b) 3D model.

Figure 2.1: *MexNext*-blade (images reproduced from (Zhang et al., 2014)).

Figure 2.1a shows the values for the dimensionless chord and the twist angle along the blade given in the report of Zhang et al. (2014). Figure 2.1b shows a 3D model of the blade from the same report. To check whether the Mexico-blade was designed properly a simple calculation for the optimum chord length distribution can be performed using [(Manwell et al., 2010b), (Schubel and Crossley, 2012) and (Muhsen et al., 2019)] :

$$C_{opt} = \frac{8\pi r}{BC_l}(1 - \cos\Phi) \tag{2.1}$$

$$C_{opt} = \frac{2\pi r}{B}\frac{8}{9C_l}\frac{U_{rated}}{\lambda\sqrt{\Omega^2 U^2}} \tag{2.2}$$

$$C_{opt} = \frac{16}{9}\frac{\pi R}{BC_l\lambda}\frac{1}{\sqrt{(\lambda\frac{r}{R})^2 + \frac{4}{9}}} \tag{2.3}$$

Equations (2.1), (2.2) and (2.3) show that the optimal chord length distribution is determined by the number of blades, three for a classic turbine, the lift coefficient, the span-wise location of the aerofoil and the inflow angle of the resultant velocity. In equations (2.2) and (2.3) the inflow angle is given by

the tip-speed-ratio (TSR). The lift coefficient is dependent on the aerofoil-type and the designed AOA of that aerofoil. As a first estimate, usually the aerofoil-type and the AOA at the tip of the blade are used. In this case the NACA 64-418. The chord-line of the aerofoil at the tip of the blade is usually in line with the plane of rotation. The report of Schepers et al. (2012) mentions that the optimal tip-speed ratio of the Mexnext-turbine is achieved at a wind speed of 15 [m/s] and a rotational speed of 100 [m/s]. From these values it is clear that the Mexnext-turbine is designed for a tip-speed ratio of 6.7. Knowing this, the inflow angle along the span of the blade can be determined using a formula derived from Manwell et al. (2010b):

$$\Phi(r) = \frac{2}{3} \arctan \frac{1}{\lambda_r} \tag{2.4}$$

Equation (2.4) relates the inflow angle (Φ) to the ratio between the tangential velocity of the blade and the free-stream velocity (λ_r). The tangential velocity depends on the span-wise location along the blade. At the tip of the blade the inflow angle is about 5.6 degrees. The report of Zhang et al. (2014) mentions the Reynolds numbers, in the order of $5 \cdot 10^5$, at which the blade is tested. From the Reynolds number and the inflow angle at the tip of the blade the lift coefficient at the tip of the blade can be determined from aerofoil data sheets. According to Airfoil Tools (2023) the lift coefficient of the NACA 64-418 aerofoil at a Reynolds number of $5 \cdot 10^5$ and an AOA of 5.6 degrees is about 0.9. To get a more accurate result, the lift coefficients of the other aerofoils used along the span of the blade can be determined using the design AOA of the aerofoil. The design AOA is the AOA at which the lift-to-drag ratio is largest. This is dependent on the Reynolds number.

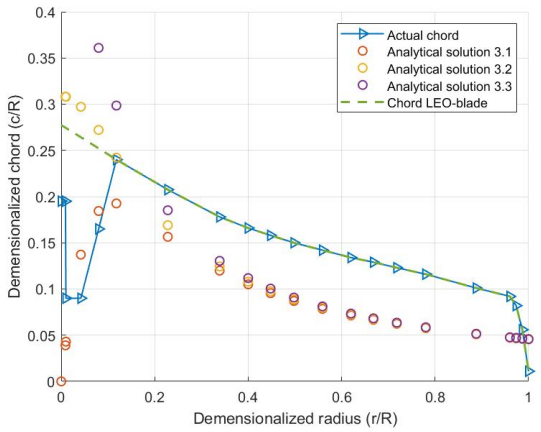

(a) Optimum dimensionless chord distribution as calculated using equations 2.1, 2.2 and 2.3 compared to the dimensionless chord.

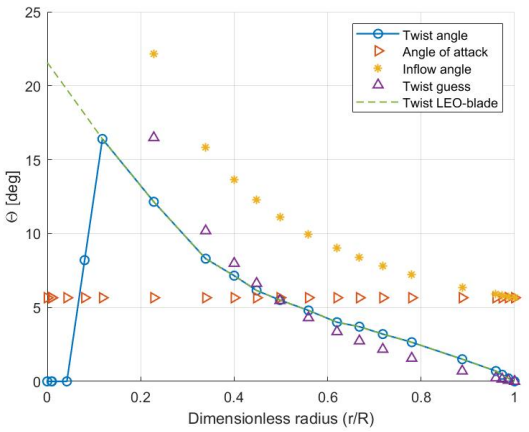

(b) Twist distribution of the *MexNext*-blade compared to initial guess and the final *LEO*-blade twist distribution.

Figure 2.2: *MexNext*-blade compared to analytical solutions and final *LEO*-blade.

Knowing that the lift coefficient at the tip of the blade is about 0.9, the optimum chord distribution is calculated using equations (2.1- 2.3). The results are compared to the chord distribution of the *MexNext*-blade as shown in Figure 2.2a. What is interesting to see is that all of the applied analytical solutions are about 50% of the actual chord length. This can be related to the blade being about two meters in length and a mistake with the y-axis title. The y-axis title should probably have been the real chord rather than the dimensionless chord. In the LEO-blade the curve has been used as a dimensionless distribution on purpose to double the Reynolds numbers and hence make the experimental turbine model more comparable to real turbines. However, the increase in chord length also increases the solidity of the turbine making it again less comparable. But the higher Reynolds numbers result in a less dynamically unstable airflow and a higher lift generation. In addition the increased chord causes a larger volume

inside the aerofoil to install the oscillating system.

$$C_{polynomial}\left(\frac{r}{R}\right) = -0.6060\left(\frac{r}{R}\right)^4 + 0.8582\left(\frac{r}{R}\right)^3 - 0.1782\left(\frac{r}{R}\right)^2 - 0.3053\left(\frac{r}{R}\right) + 0.2773 \quad (2.5)$$

Figure 2.2a shows the dimensionless chord distribution of the *LEO*-blade compared to that of the *MexNext*-blade. As can be seen in Figure 2.2a, a change has been made to the root of the blade. The curve for the chord distribution has been extended to the root of the blade using the fourth order polynomial shown in equation 2.5. A fourth order polynomial is used as it gives a smooth transition between the existing curve and the new root. The *MexNext*-blade uses cylinder foils to attach the blade to the nosecone. However, since the *LEO*-blades are smaller and the nosecone bigger, the root of the blades have a more significant impact on the generated lift. Hence it is decided to extend the base aerofoil to the root of the blade.

$$\Theta_{polynomial}\left(\frac{r}{R}\right) = -98.2567\left(\frac{r}{R}\right)^4 + 133.8557\left(\frac{r}{R}\right)^3 - 21.7025\left(\frac{r}{R}\right)^2 - 42.6817\left(\frac{r}{R}\right) + 21.5652 \quad (2.6)$$

As explained in the introduction of this report, the twist angle is the angle between the inflow angle and the AOA of the aerofoil. As the inflow angle decreases along the span of the blade, so does the twist angle. A first estimate for the twist distribution can be made by subtracting the AOA at the tip of the blade from the inflow angle. As discussed before, the twist angle at the tip of the blade is equal to zero. Consequently, the AOA at the tip of the blade is equal to the inflow angle at the tip of the blade. Again, to get a more accurate result the design angles of attack for the other aerofoils used along the span of the blade can be implemented in the calculations. The TSR of 6.7 of Schepers et al. (2012) results in an inflow angle and hence an AOA of about 5.6 degrees at the tip of the blade. Figure 2.2b shows the twist distribution of the *MexNext*-blade compared to the initial twist guess using the inflow angle. As can be seen, the initial guess is close to the used twist distribution and hence the twist distribution is considered accurate. Since the *LEO*-blade also aims to operate at a TSR of about 7, the twist distribution is kept the same except again for the change at the root of the blade. The twist distribution is, just like the chord distribution, extended to the root of the blade using the fourth order polynomial shown in equation 2.6. Designing a wind turbine for a TSR of 7 to 8 is a requirement when designing an efficient wind turbine. It is well known that the real efficiency of a three bladed turbine peaks at a TSR of about 7 to 8. However, during the experiments the aim is to get a lower TSR of about 3.5 to 4.5 to induce an AOA of about 8 degrees. This is because at the Reynolds numbers experienced by this blade, below 10^5, the peak of the lift-over-drag ratio is shifted from 5 degrees to about 8 to 10 degrees. Hence, the dynamic stall effect could have more influence at these increased angles of attack.

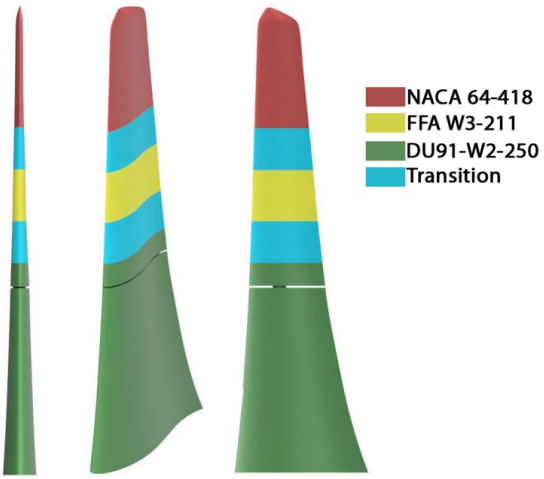

Figure 2.3: 3D model of the original *LEO*-blade design showing the used aerofoils across the span of the blade (image reproduced from (Schweickert, 2016)).

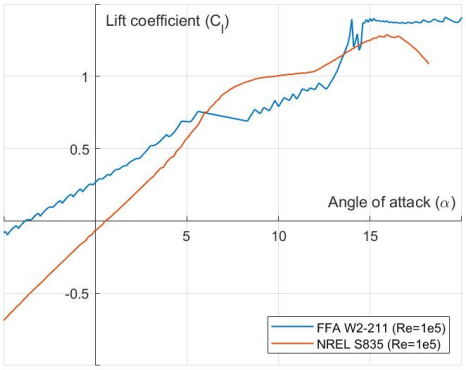

Figure 2.4: Lift coefficient versus AOA curves for the *FFA W2-211* and *NREL S835* aerofoils at a Reynolds number of $1{\cdot}10^5$.

Figure 2.1b shows the aerofoils used in the *MexNext*-blade. In the original design of the *LEO*-blade the *RISO-A1-21* aerofoil was replaced by the *FFA W2-211* aerofoil due to availability issues of the *RISO-A1-21* aerofoil data. Figure 2.3 shows the 3d model and the used aerofoils of the original *LEO*-blade design. In the new *LEO*-blade design the *DU91-W2-250* and the *FFA W2-211* aerofoils are both replaced by the *NREL S835* aerofoil. This is because the latter aerofoil is actually specifically designed for the scale of this turbine, whilst the original aerofoils are not. *XFOIL* simulations show that at a Reynolds number of about $1{\cdot}10^5$, which is already larger than the Reynolds numbers experienced by the *LEO*-blade, the *DU91-W2-250* and the *FFA W2-211* aerofoils show a saw-tooth behaviour in the lift-coefficient curves. The saw-tooth behaviour is caused by convergence issues, which in turn could be caused by unsteady aerodynamics. According to Gudmundsson (2014) *XFOIL* combines a high-order panel method with a fully coupled viscous-inviscid interaction method to compute drag, boundary layer transition and separation. Bauer (2021) states that *XFOIL* uses one of the many simplifications of the *Navier-Stokes* equations which only works as long as no large separation bubbles or other strongly non-linear effects occur anywhere. Hence, this might be happening to the *DU91 W2-250* and *FFA W2-211* aerofoils at lower Reynolds. Figure 2.4 shows the lift-coefficient curves for the *FFA W2-211* and *NREL S835* aerofoils at a Reynolds number of $1{\cdot}10^5$. As can be seen from the figure, the *NREL S835* aerofoil does not show the unsteady saw-tooth behaviour at the lower Reynolds numbers and is hence more suitable for the *LEO*-blade.

2.2 Design of the oscillating flap

This section elaborates upon the design of the oscillating flap. First the optimal span-wise location is determined to generate the most lift. Next the bending aerofoil is designed by calculating the required thickness. Section 2.2 ends with a description of the oscillating mechanism.

2.2.1 Design of the flap

To exploit most of the performance increase, the flap should be added to the location along the blade which produces the most lift. The useful tangential force generated by an aerofoil is dependent on the density of the fluid, the resultant velocity, the lift coefficient and the lift-to-drag ratio. The total

tangential force over the rotor is then the integral of the tangential force along the span of the blade multiplied by the number of blades. The resultant velocity at the root of the blade is relatively low and hence the generated lift is low too. The tip of the blade has the highest resultant velocity and should hence produce the most lift. However, to reduce tip vortices and to reduce the noice produced at the tip, the lift coefficient and the lift-to-drag ratio at the tip are reduced significantly by reducing the twist angle as well as the chord length to zero. This results in an AOA far below the optimal AOA and hence a reduction in the lift coefficient and lift-to-drag ratio. Consequently, the generated lift both at the root and the tip converge to near zero and the highest amount of generated lift is actually somewhere along the blade.

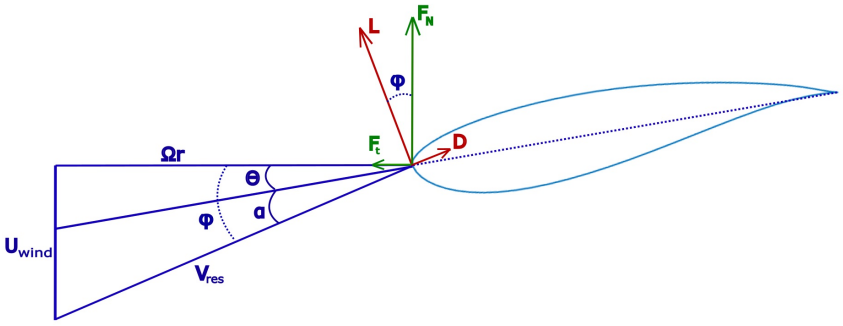

Figure 2.5: Tangential force acting on an aerofoil

$$\delta F_t = {}^1\!/_2 \rho c B V_{res}^2 C_l \left(\sin \Phi - \frac{\cos \Phi}{C_l / C_d} \right) \cdot \delta r \tag{2.7}$$

Figure 2.5 shows how the tangential force depends on the lift and drag. As shown in Section 2.1 the AOA along the span of the blade is relatively constant. Hence a good approximation of the lift distribution along the span of the blade can be made by filling in the lift coefficient values of the *NREL S835* and *NACA 64-418* aerofoils. The values are gathered from Airfoil Tools (2023) and the curves are generated using equation (2.7).

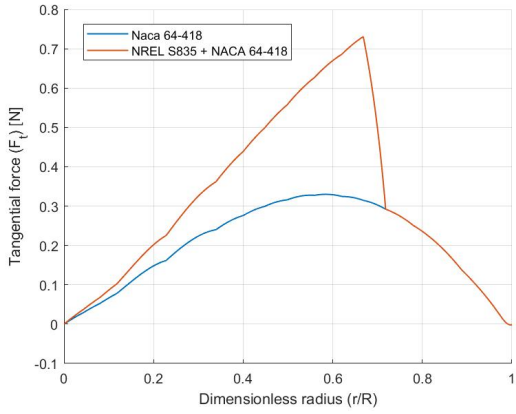

Figure 2.6: Distribution of the tangential force along the span of the blade.

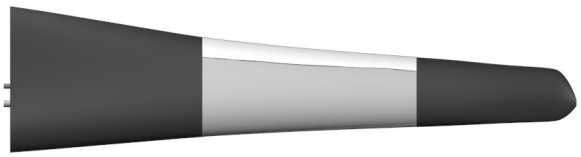

Figure 2.7: Front view of the 3D model of the new *LEO*-blade design

Figure 2.6 shows an example of the tangential force distribution over the span of the *LEO*-blade. These are by no means the exact values for the *LEO*-blade. The blue line represents the distribution if only the lift and lift-over-drag coefficients of the tip aerofoil are used. The orange line represents the distribution if the coefficients of the root and mid-span aerofoil are added as well. Figure 2.6 clearly shows that the

peak of the lift is generated at about 0.6 to 0.7 of the span and that most of the total lift is generated between 0.3 and 0.7 of the span. Hence, it is decided to design the flap between 0.3 and 0.7 of the blade span. Figure 2.7 shows a 3D model of the blade. In white is shown the oscillating flap and in dark grey the static root and tip of the blade. A more accurate prediction on the lift distribution could be made by simulating the exact lift coefficient for each Reynolds number along the span of the blade. This is, however, not the goal of this calculation. The goal is to find the general shape of the lift distribution to determine the optimal location of the flap. For this, the general prediction using only two lift coefficients is accurate enough. This is because more accurate lift coefficients would only increase, or decrease, the steepness of the curve and not so much change the location of the peak. This, in turn, is explained by the fact that the lift coefficients are dependent on the Reynolds numbers, where a decrease in Reynolds number decreases the lift coefficient. The Reynolds number peaks at about 0.8 dimensionless radius, but since this part of the blade is already covered by the less efficient *NACA 64-418* aerofoil the peak of tangential force distribution, as shown in Figure 2.6, would not be able to shift toward the right.

In addition to the location of the flap the design of the oscillation mechanism can have a significant influence on the success of the Albatrozz technology. Prior experience with CFD within the bio-mimetic research group has shown that a small discontinuity, like a gap, would be detrimental for the performance of the airfoil. This needs to be taken into consideration in the design process.

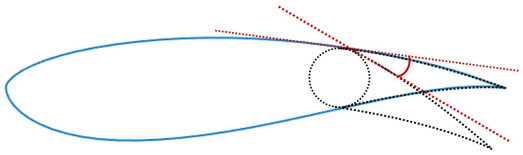

Figure 2.8: Acute angle between static aerofoil and rotating flap

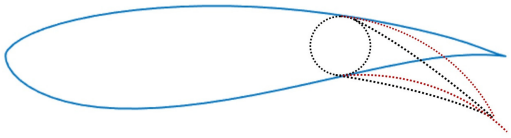

Figure 2.9: Rotating flap (black) versus a bending flap (red)

To make sure no discontinuities are present in the airfoil it is decided to design a bending mechanism. In addition, if the oscillating flap creates an acute angle between the continuous line of the static part of the aerofoil and the flap, as shown in Figure 2.8, the chance of the airflow detaching from the aerofoil is increased. A bending mechanism, using flexible Thermoplastic Polyurethane (TPU), could discard this chance by allowing for a curvature along the flap. Figure 2.9 shows the difference between a rotating and a bending flap. A bending flap should create a more attached airflow. The required thickness along the length of the flap to achieve this curvature can be estimated by the Euler-Bernoulli beam theory. The Euler-Bernoulli beam theory can actually only be used for infinitely small deflections, however the extended version can be used for larger deflections provided that the Karman-strains remain small (Reddy, 2008).

For a bending flap to work, the wall that faces the lower pressure (LP) zone needs to be disconnected from the wall that faces the higher pressure (HP) zone at the TE. This is to make sure that the wall that faces the HP side is able to move freely underneath the LP wall. If the walls were to be connected at the trailing edge, the HP wall would curl up into the open space inside the aerofoil and this could create a pocket in the surface of the aerofoil.

The Euler-Bernoulli beam theory states that the required thickness along a beam is dependent on the moment and the curvature. The moment generated along the beam is determined by the driving mechanism of the oscillatory motion. Different methods induce different moments in the beam. During the design of the flap, two driving mechanisms were explored: bending by pulling horizontally on the TE and bending by pushing down on the TE using a rotating arm. One thing to clearify is that other methods the bend the flap, like piëzo-/thermal-electric actuators or pressurised chambers like done in the paper of Madsen et al. (2015) do exist. However, commonly available piezo-electric actuators do not have the ability to perform the required deflection and the pressurised chambers from Madsen et al. (2015) would be too complex for the rotating system.

$$\frac{a}{\sin\alpha} = \frac{b}{\sin\beta} = \frac{c}{\sin\gamma} = 2r \tag{2.8}$$

$$r_{original}(x_i) = \frac{\sqrt{(x_i - x_{i-1})^2 + |y_i - y_{i-1}|^2}}{2\sin(\beta - \epsilon)}) \tag{2.9}$$

$$\beta = \arctan\left(\frac{|y_{i+1} - y_{i-1}|}{x_{x+1} - x_{i-1}}\right)$$
$$\epsilon = \arctan\left(\frac{|y_{i+1} - y_i|}{x_{i+1} - x_i}\right)$$

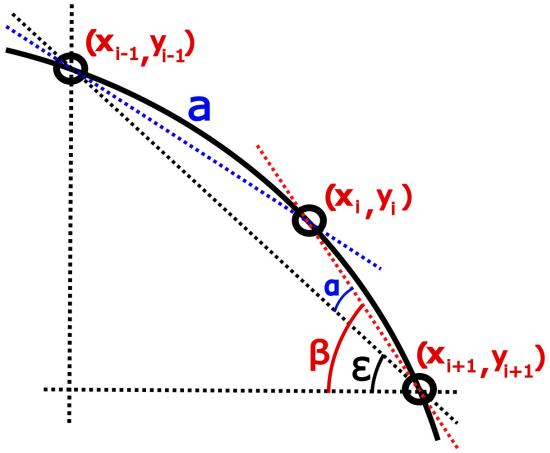

Figure 2.10: Calculating the radius of the curvature using the sine rule.

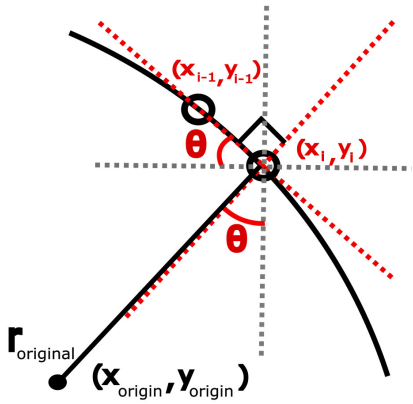

Figure 2.11: Determining the *(x,y)*-origin of the curvature.

Calculating the required thickness of a straight beam is rather straightforward. First the required deflection needs to be determined, from which the resulting moments and required thickness can then be calculated. An aerofoil however, already has a curvature which needs to be subtracted from the final curvature to get the correct bending of the aerofoil. Hence the first step is to determine the original curvature of the flap using equation (2.9) which is derived from the sine rule shown in equation (2.8). Since the coordinates of the flap are known, the angles and the distances between the coordinates can be determined as shown in Figure 2.10. Length *a* is determined using Pythagoras on the *(x,y)*-coordinates of the to be calculated radius, (x_i,y_i), and the previous coordinates (x_{i-1},y_{i-1}). Next the radius at point *i* can be calculated by dividing length *a* by two times angle α, where angle α is the difference between angle β and ϵ. These angles are calculated using goniometrics on the aerofoil coordinates.

$$\theta(x_i) = \arctan\left(\frac{|y_i - y_{i-1}|}{x_i - x_{i-1}}\right) \tag{2.10}$$

$$x_{origin,i} = x_i - (r_{original}(x_i) \cdot \sin(\theta(x_i))) \tag{2.11}$$

$$y_{origin,i} = y_i - (r_{original}(x_i) \cdot \cos(\theta(x_i)) \tag{2.12}$$

The second step is to determine the *(x,y)*-origin of the original radius at point *i*. For this step it is assumed that the distance between two coordinates compared to the radius of the curve is so small, that the curve between the two coordinates can be described as a straight line. The angle θ, as shown in Figure 2.11 and calculated with equation (2.10), can then be used to determine *(x,y)*-origin using equations (2.11) and (2.12). These equations again use simple goniometrics on the known coordinates.

$$\gamma(x_i) = \arctan\left(\frac{|y_{i+1} - y_{origin,i}|}{x_{i+1} - x_{origin}}\right) \tag{2.13}$$

$$L_(x_i) = \frac{90 - \gamma(x_i) - \theta(x_i)}{360} 2\pi r_{original}(x_i) \tag{2.14}$$

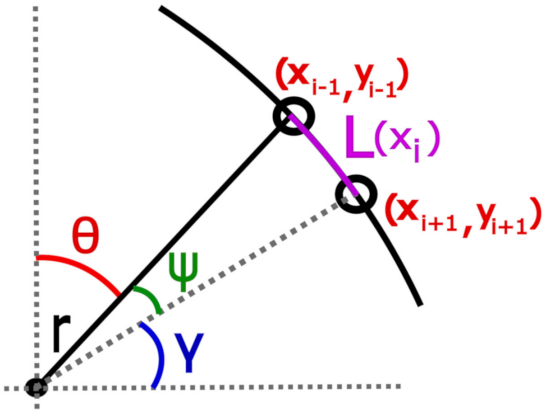

Figure 2.12: Length of arc-piece

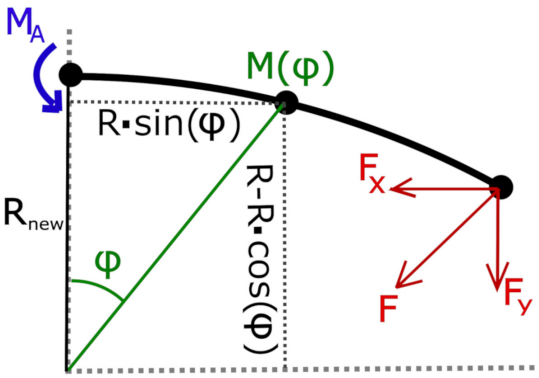

Figure 2.13: Moments induced in the flap

In the third step the angle γ, as shown in Figure 2.12, is calculated using equation (2.13). This angle, in addition to angle θ, is subtracted from 90 to get the angle ψ which describes the angle between two coordinates. Angle ψ is then used to calculate the arc-length described between the two coordinates using equation (2.14).

$$r_{minimum} = \frac{2\sum L_(x_i)}{\pi} \tag{2.15}$$

Knowing the arc length between each coordinate, the sum of the arc lengths can then be used to determine the minimum radius which could be described by the total arc length. Equation (2.15) shows the minimum radius needed to describe a quarter of a circle or $^1/_2 \cdot \pi$.

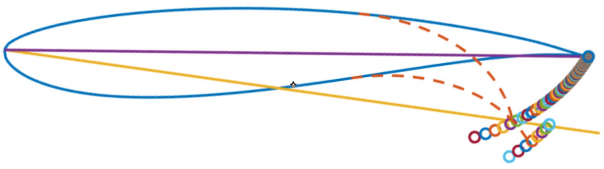

Figure 2.14: Possible curvatures that can be drawn with length L shown as colored circles representing the location of the TE.

Using a *for-loop*, multiple possible curvatures are drawn in between the original curvature and the minimum curvature. The research of Neven (2020) has shown that an increase in AOA of about 10^o is a good value to induce dynamic stall. Hence, for this design the aim is to be able to have a maximum change in AOA between the LE and TE of about 10^o. A line with an angle of 10^o with respect to the chord-line is drawn from the LE. The curvature of which the end point intersects with this line is the curvature that can achieve this angle. Figure 2.14 shows the curvature needed to get a change in AOA of 10 degrees. The colored circles represent the location of the TE for each of the curvatures that can be drawn with the length of the flap.

$$M(\phi_i) = M_A + F_x \cdot (R_{new} - (R_{new} \cdot \sin\phi)) + F_y \cdot R_{new} \cdot \sin\phi_i \tag{2.16}$$

$$\rho(x) = \frac{1}{r(x_i)} \tag{2.17}$$

$$b(x_i) = \sqrt[3]{\frac{12 \cdot M(\phi_i) \cdot \frac{1}{\rho_{original}(x_i) - \rho_{new}}}{h \cdot E}} \tag{2.18}$$

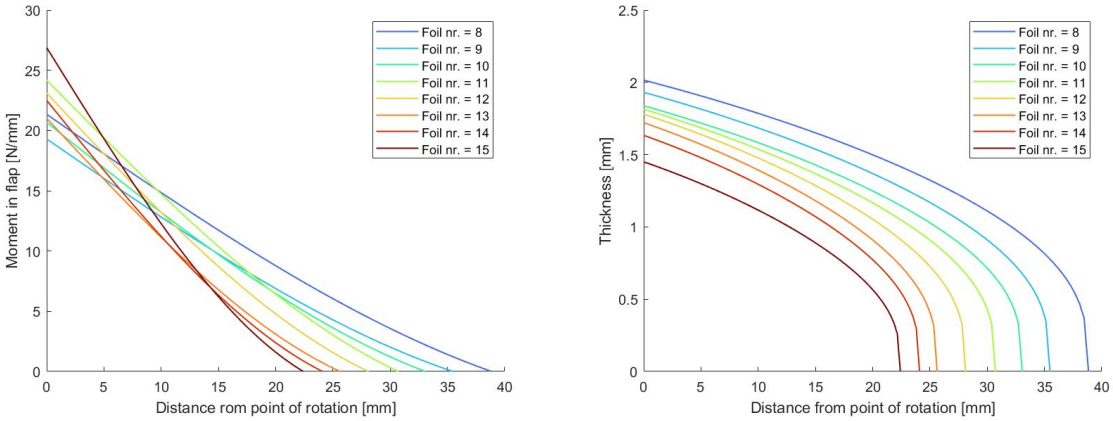

(a) Induced moments (b) Required thickness

Figure 2.15: LP side flap going from the point of rotation to the TE.

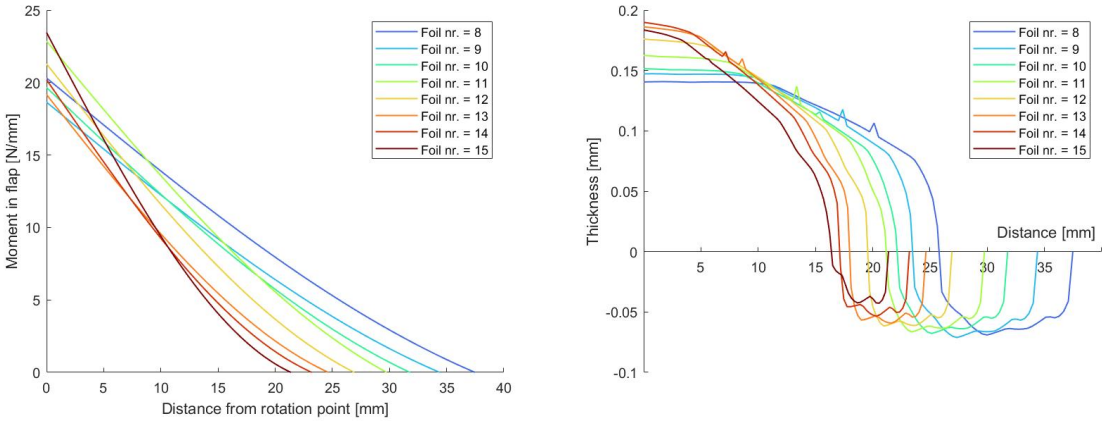

(a) Induced moments (b) Required thickness

Figure 2.16: HP side flap going from the point of rotation to the TE.

Knowing the required curvature, the bending moments in the flap can then be determined using equation (2.16). Where M_A is the bending moment where the flap starts bending, F_x and F_y are the forces in the x- and y-direction respectively, R_{new} is the radius after bending and angle Φ is the angle between the origin of the circle described by R_{new} and the location i. As stated before, bending of the flap can be achieved through two methods, either by pulling the trailing edge (TE) towards the oscillating axle or by connecting the TE to the driving axle using a stiff beam. The first option in combination with springs is used in the larger scale test turbine. The springs are added to lower the input energy by oscillating the flap at the resonance frequency of the springs. Unfortunately, due to the scale of the wind tunnel

setup this system is unfeasible and the TPU is not stiff enough to oscillate at a high frequency on its own. According to Noffke (2011) high frequencies, in the range of 10 to 15 [Hz], are needed to achieve the positive effect of dynamic stall. This will be further elaborated in Section 2.4. For the experimental scale turbine the decision is made to pull the TE downwards using rotating rods. Now the direction of the force is known, but the value is not. Unfortunately both the force is required to determine the required thickness and the thickness to determine the required force. Hence it is opted to fill in arbitrary values such that the flap is thin enough to create enough space for the oscillating mechanism, yet thick enough to be easily 3D-printable. Equation (2.18) shows the used formula, derived from the *Euler-Bernoulli beam theory*, to determine the required thickness of the high pressure (HP) and low pressure (LP) side flap. As stated before, the required thickness is dependent on the final curvature minus the original curvature, the moments experienced at each point along the flap ($M(\Phi)$), the length of the flap in span-wise direction (h) and the Young's modulus (E) of the material. In this sense, the curvature is the inverse of the radius, as shown in equation (2.17). Figures 2.15a and 2.16a show the resulting moments along the length of the LP and HP side flap respectively. Figures 2.15b and 2.16b show the final required thickness of the LP and HP side flap. Important to notice from Figure 2.16b are the negative values for the thickness close to the TE. This phenomenon originates from the fact that, close to the TE the original radius of the unbend aerofoil is smaller than the radius of the final, maximum deflected, aerofoil. As the curvature is the inverse of the radius, the curvature of the unbend aerofoil ($\rho_{original}$) becomes larger than the curvature of the deflected aerofoil (ρ_{new}) and hence the thickness calculated in equation (2.18) becomes negative. This can be rationalized by the fact that close to the TE, the flap has to be straightened as opposed to bend to create the desired curvature. For the final model these negative values are not a problem because the TE is too thin to be used by the LP and HP flap simultaneously. The LP flap extends to the TE and the separation between the LP and HP flap is made at the HP side before the values become negative.

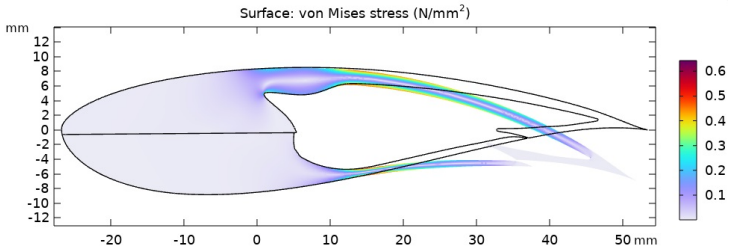

Figure 2.17: Von misses stresses in the LP and HP side flaps.

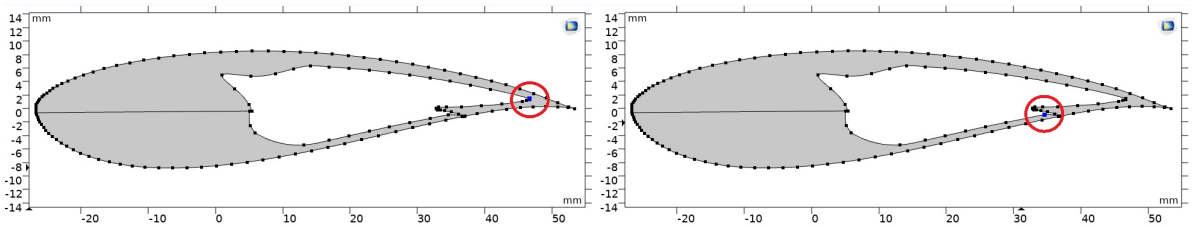

(a) LP side flap

(b) HP side flap

Figure 2.18: Connection points solid mechanics.

Figure 2.17 shows the stresses within the LP and HP side flaps. The simulated deflection is about 7.8 degrees. The scale of the stresses goes up to about 0.63 [N/mm^2], which is well below the maximum allowable stress of 67 [N/mm^2] for TPU. Hence, it can be concluded that the flaps will not break during the experiments. The simulation is performed in *Comsol Multiphysics 6.0* using a solid mechanics prescribed displacement of -5.3 [mm] on the LP side flap and a prescribed displacement of -3.3 [mm] on the HP side flap. Both displacements are in the vertical direction and the connection points are shown in Figures 2.18a and 2.18b respectively. The horizontal connecting line between the LP and HP side flap

acts as a fixed constraint. The material used for the simulation is TPU with a density of 1210 [kg/m^3], a Young's modulus of 67 [MPa] and a Poisson's ratio of 0.3897. The mesh used is a *Comsol Multiphysics 6.0* generated fine mesh.

2.2.2 Design of the oscillation mechanism

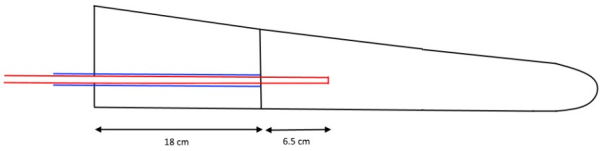

Figure 2.19: Original 2D design of oscillating mechanism of the *LEO*-blade (image reproduced from (Mahfoozi, 2020)).

In the previous versions of the *LEO*-blade, the outer half of the blade was oscillated around the $^1/_3$ chord-line, which is also the pitching axis of the blade, whilst the inner half was static. Figure 2.19 shows the original oscillating mechanism of the *LEO*-blade. The oscillatory motion was driven by a tail rotor from a remote controlled toy *Vario* helicopter. This system is also implemented into the new design.

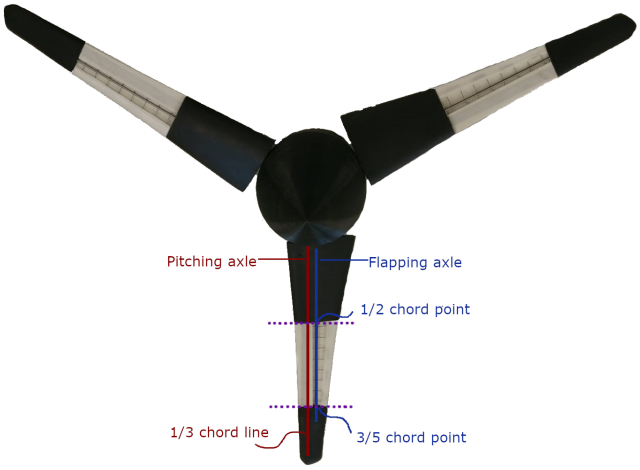

Figure 2.20: Assembly of the turbine showing the pitching axle at the $^1/_3{}^{rd}$ chord line and the driving axle of the flapping system parallel to the pitching axle.

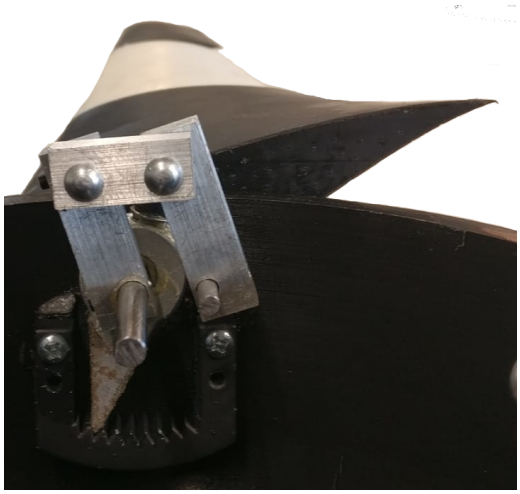

Figure 2.21: Pitching system and lever arms connecting the tail rotor to the axle driving the TE flap.

In the new design only a flap on the trailing edge is oscillated. This flap does not oscillate around the $^1/_3{}^{rd}$ chord-line, but rather between $^1/_2$, for the foil closest to the root, and $^3/_5{}^{th}$ of the chord-line for the foil closest to the tip of the blade. This value varies along the length of the flap to keep the axis of rotation of the flap parallel to the axis of rotation of the tail rotor. During the design process the question arose if the varying of the length of the flap in chord-wise direction, as a result of the varying location of the axis of rotation along the length of the blade, has a significant influence on the efficiency of the induced dynamic stall effect. This question is answered in Section 3.2.

As stated previously, the axle that drives the oscillatory motion is not in line with the axis of rotation of the tail rotor. Hence, a connecting lever arm is required as can be seen in Figure 2.21. In the previous design the blades were friction mounted by clamping the axles of the blade in between two thick aluminum rings. To make room for the lever arms in the new design these rings had to be removed and a different mounting system had to be designed. This is further explained in Section 2.3.

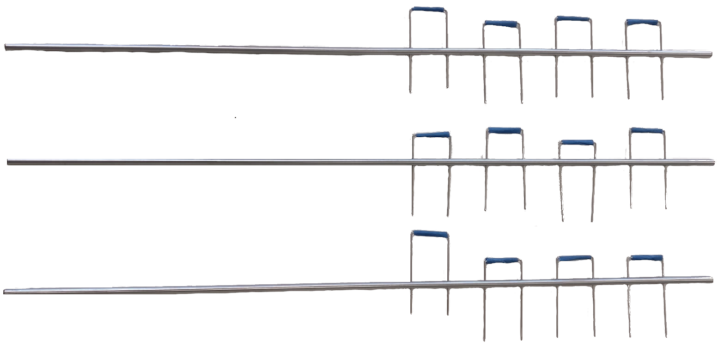

Figure 2.22: Driving axles of the oscillatory motion with the stiff rods going through holes in the axle.

As stated in Section 2.2.1 the flapping motion is achieved by connecting the TE with the driving axle through stiff rods. It is also stated that an acute angle between the stiff part of the aerofoil and the flap could lead to delaminizing of the airflow resulting in a less effective dynamic stall. Hence, flexible TPU is used to force the flap into a curvature. As the flap moves downwards, the radius of the curvature and the distance between the TE and the driving axle decreases. A stiff connection of the rod to both the TE and the driving axle would not allow this. Hence, holes are added to the driving axle through which the rods can slide up and down. Figure 2.22 shows the driving axle with the stiff rods. The holes are not in a straight line, but rather at a small angle to accommodate for the twist in the blade.

2.3 Design and safety of the nosecone assembly

As stated in Section 2.2.2 the thick aluminum rings used in the previous design to hold the blades had to be removed to make room for the lever arms. These aluminum rings were used as it was believed that the resin, from which the nosecone was made, would be too brittle to withstand the forces needed to hold the blades using friction. This Section elaborates more upon the design changes to mount the blades onto the nosecone as well as the shape of the nosecone.

(a) Tooth of the pitching arm interlocking with counter teeth on the nosecone.

(b) Pitching arm shown connected to the blade.

Figure 2.23: Pitching mechanism of the blades.

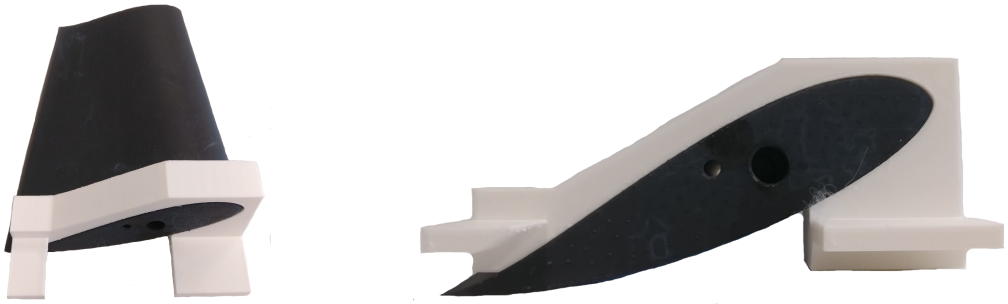

(a) Side view (b) Bottom view

Figure 2.24: Zero pitch angle guide.

(a) Top view (b) Side view

Figure 2.25: Setting the zero pitch angle.

In the new design the blades are mounted using shear and tension rather than friction. The outside dimensions of the nosecone, 180 [mm] diameter, are kept the same as the previous design to allow for equal comparison of the results. The material of the nosecone is replaced with tough PLA and the thickness is reduced from 10 [mm] to 5 [mm]. Just as in the previous design, a 9 by 6 [mm] tube is glued at the $1/3$ chord-line. This tube is the anchor point of the blades to the nosecone. In the tube is a 5.5 [mm] rod that is connected to the tail rotor. Within the nosecone an aluminum arm is connected with a setscrew to the tube. As can be seen in Figures 2.21, 2.23a and 2.23b at the end of this arm is a tooth which interlocks with another tooth on the nosecone. This allows for accurately setting the blade pitch angle. Small changes in pitch angle can be achieved by swapping the nosecone teeth for a different configuration. The turbine has a pitching range of -5 to 30 degrees and the zero degree pitch angle is accurately set using a 3D printed negative of the root foil which is shown in Figures 2.24a, 2.24b, 2.25a and 2.25b.

$$F_c = m\omega^2 r \tag{2.19}$$

As the turbine spins, a centrifugal force force acts on the blades causing them to put a radial outward force on the connection point. Using the formula for centrifugal force, equation (2.19), a maximum rotational speed of 700 rpm, a mass of approximately 600 [g] and a centre of gravity at approximately $1/3$ of the blade length, or 24 [cm] from the axis of rotation, the centrifugal force acting on the blade is approximately 775 [N]. In the new design a tensile force in the nosecone created by the arm of Figure 2.23a counteracts this centrifugal force. The arm has a surface area of approximately 545 [mm^2] resulting in a tensile stress of about 1.42 [MPa]. Using a safety factor of 10 the used material should be able to withstand a stress of at least 14.2 [MPa]. According to Ultimaker (2022) 3D printed tough PLA should be able to withstand tensile stresses up to 33 to 47 [MPa] depending on orientation of printing.

3D printed parts are often prone to shearing of the layers. The arm has a circumference of about 105 [mm] and the thickness of the nosecone is about 5 [mm]. This creates an area of shear of about 525 [mm^2], hence resulting in a shear force on the nosecone of about 1.48 [MPa]. Again, using a safety factor of 10 the nosecone should be able to withstand a shear force of 14.8 [MPa]. The allowable shear force of a material is not usually given, but can be assumed to be about 60% of the ultimate tensile strength (Budinski, 2014). This would result in a shear strength of about 19.8 to 28.2 [MPa] depending again on the orientation of printing.

The tube that hold the blades is held in place with the aluminum arm from Figure 2.23a using a 4 [mm] set screw. This set screw is bolted into a small hole creating a tensile stress in the tube as well as a shear stress in the set screw. As said before the outside diameter of the tube is 9 [mm] and the inside is 6 [mm], minus the area of the 4 [mm] set screw results in a tensile area of about 29 [mm^2]. Consequently, the tensile stress in the tube is about 26.7 [MPa] with a safety factor of 10 results in a minimum allowable tensile stress in the tube of about 267 [MPa]. The tube is made from silversteel with a tenstile strength of about 750 [MPa]. The set screw is made from hardened steel class 12.9 and will subjected to a shear stress of about 61.7 [MPa]. Using a safety factor of 10 results in a shear stress of 617 [MPa]. Again assuming a shear strength of 60% of the ultimate tensile strength results in a maximum allowable shear stress of 720 [MPa].

Another failure point is the glue between the 9 [mm] tube and the root of the blade. The tube is glued into a hole with a depth of 65 [mm], hence the total surface area is about 1838 [mm^2]. If the whole surface area of both the tube and the root of the blade is in contact with the glue, then the maximum stress within the glue when accounting for the safety factor is about 4.2 [N/mm^2]. The epoxy has a rated strength of 17.7 [N/mm^2] and hence it should be safe.

Table 2.1: Stresses at the failure points within the turbine assembly.

Failure point	Force [N]	Area [mm^2]	Safety factor	Calculated stress (with SF) [MPa]	Allowable stress [MPa]	Stress below failure?
Normal stress nosecone	775	545	10	14.2	33-47	Yes
Shear stress nosecone	775	525	10	14.8	19.8-28.2	Yes
Normal stress tube	775	29	10	267	750	Yes
Shear stress set screw	775	12.6	10	617	720	Yes
Glue between tube and blade root	775	1838	10	0.42	17.7	Yes

Table 2.1 summarizes the calculated and maximum allowable stresses at each of the possible failure points within the design. The calculations on the shear and tensile stresses in this section have shown that none of the possible failure points should reach their respective maximum allowable stresses and hence the design can be considered safe to operate.

2.4 Wind tunnel test setup

In this Section the test setup is explained in detail to allow for repeatability of the performed tests. In addition, the results can be accurately analysed if the setup and the conditions are well defined. In the Section 2.4.1 the overview of the wind tunnel is described and in Section 2.4.2 the performed tests are defined.

2.4.1 Overview of the test setup

To test the theory on the Albatrozz flaps, three pieces of the designed blade are manufactured and connected to a *'Turnigy HD 5206 BLDC brushless gimbal generator'*. The classical three bladed one meter diameter scale wind turbine model is then added to a closed wind tunnel to test the response of the model under various conditions. A schematic overview of the tunnel can be seen in Figure 2.26. The tunnel consists of three tests sections of which the largest, on the far right, is a cube with dimensions of 1.4 by 1.4 by 1.4 meter. This is where the wind turbine model is tested. The other sections are progressively smaller. The wind speeds that can be achieved in the largest section range from 0 to approximately 4.5 [m/s]. The wind speed is measured by a Pitot tube at the smallest of the three sections.

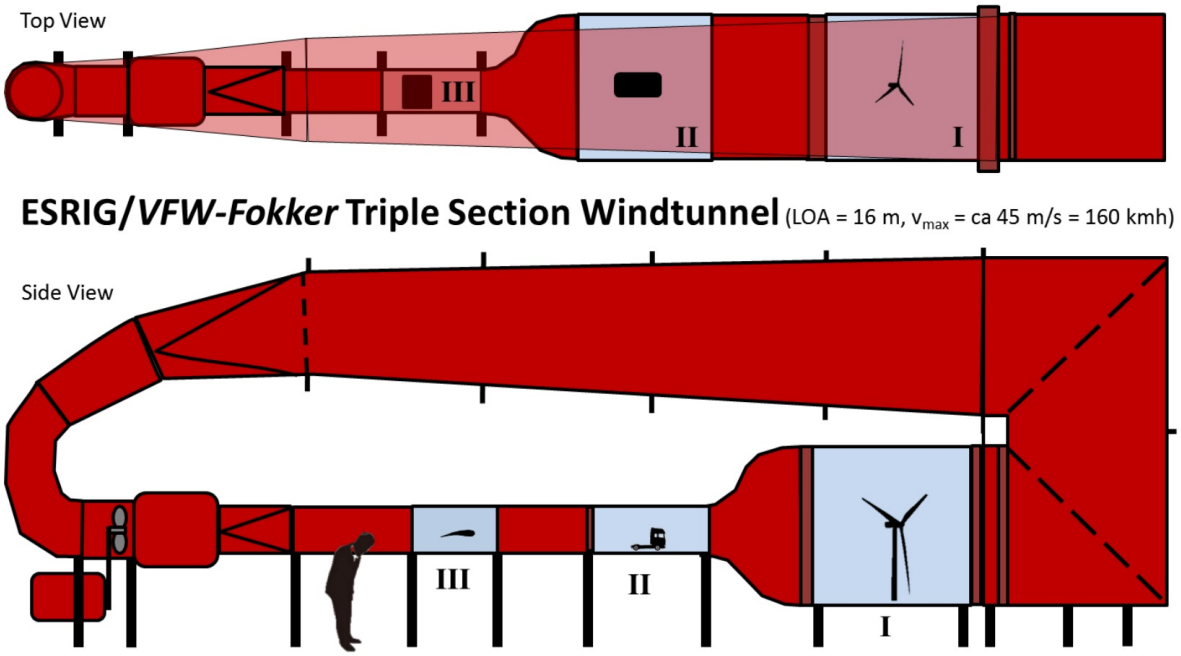

Figure 2.26: Schematic overview of the closed wind tunnel (image reproduced from Neven (2020)).

The energy created by the generator flows to a delta configured resistance where it dissipates as heat. There are five delta configured loads available from the previous test setup. These loads consists of 1, 5, 10, 50 and 100 [Ω] resistors.

$$\Omega(RPM) = \frac{60f}{n} \tag{2.20}$$

To accurately determine the performance of the turbine the frequency as well as the current and voltage over the load are measured. The frequency is measured using an oscilloscope, whilst the current and voltage are measured using a multi-meter. The measured data from the multi-meters is logged in an excel file.
Before the experiments, a few test runs are performed at low rotational speeds. The rotational speed of the turbine is measured using a *'Voltcraft'* tachometer. The measured frequency from the oscilloscope is then divided by the rotations per second, as shown in equation (2.20), to get the amount of pole pairs. A few test runs have shown that the number of pole pairs in the generator is seven, which is half of the number of magnets in the generator. Hence, we can conclude that the oscilloscope works as intended.

$$I_{wye,ph} = I_{wye,l} \tag{2.21}$$

$$V_{\Delta,ph} = V_{\Delta,l} \tag{2.22}$$

$$V_{wye,ph} = \frac{V_{wye,l}}{\sqrt{3}} \tag{2.23}$$

$$P_{wye} = 3 \cdot V_{ph} I_{ph} \tag{2.24}$$

The measured current and voltage are dependent on the configuration of the load. As mentioned before, a delta configuration of resistors is used for the load whereas a wye configuration is used in the gimbal generator. The different configurations in the generator and in the load result in different values for the phase voltages and currents. The measured current is the line current in between the generator and the load. The measured voltage is the phase voltage over one of the three phases of the load. To determine the power generated by the turbine the phase values of the *wye*-configuration are required. Equation (2.21) states that the phase current in a *wye* configuration is equal to the measured line current and equation 2.22 states that the measured phase voltage of the delta configured load is equal to the line voltage. Equation (2.23) states that the phase voltages of a *wye* configuration is equal to the line voltage divided by the square root of three. Finally, the power output is calculated using equation (2.24) which states that the generated power is equal to three times the phase voltage and current.

2.4.2 Overview of the performed tests

The performance of the scale wind turbine model is dependent on a number of variables. First of all the load. Just like any other electrical device, the gimbal generator has an unknown specific relation between the power delivered to the supplied load with an optimum power performance at an unknown specific load. As stated in Section 2.4.1 a total of five different delta configured loads are available.
In the first set of measurements each of the loads are tested for the full range of wind speeds. The measured data for each of the wind speeds is logged for 60 seconds to make sure steady-state is reached in the tunnel as well as the turbine. During these measurements the flaps are not turned on as they act as a baseline for the general performance of the static blades. In addition to the five different loads, also various blade pitch angles are tested. As stated in Section 2.1, the goal of these measurements is to find a load and pitch configuration which results in an AOA of about eight degrees. This is done to make sure that during the oscillating measurements, the AOA is driven past the point of steady-state stall. At the Reynolds numbers experienced by this blade, the steady-state stall occurs somewhere between 14 and 18 degrees AOA.

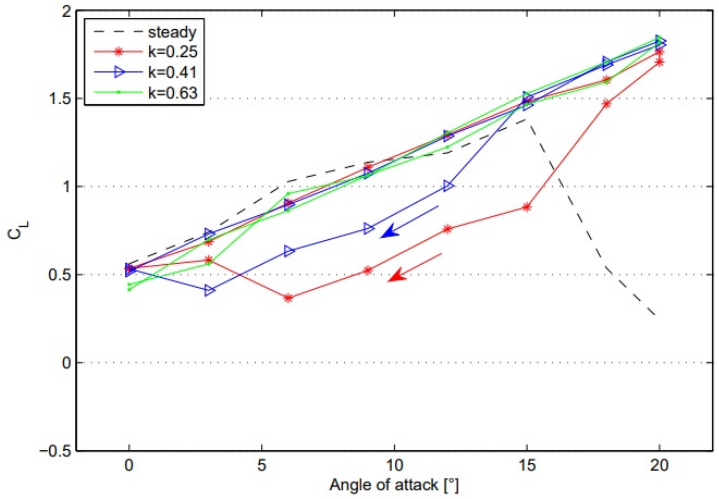

Figure 2.27: Dynamic stall of a 3D Fulmar profile (image reproduced from Noffke (2011)).

$$\kappa = \frac{2\pi f \cdot c}{U_\infty} \tag{2.25}$$

In the second set of measurements performance of the turbine using the oscillating flaps is measured. These measurements are compared to the baseline measurements to determine the overall increase or decrease in performance. As the frequency of the oscillations is a key factor for the resulting dynamic stall behaviour, a range of frequencies from 1 to 13 [Hz] are tested for each of the wind speeds. These values are derived from the reduced frequency researched in the report of Noffke (2011). The reduced frequency, as shown in equation (2.25), describes the Strouhal number when an aerofoil fulfils an angular motion. When the Strouhal and Reynolds number are kept constant, the flow around an identical aerofoil is similar even when parameters like the chord length (c), wind speed(U_∞) or oscillation frequency (f) are changed. The book of Vogel and Savage (1996) states that for a reduced frequency of $\kappa > 0.05$ unsteady effects within the flow become significant. The research of Noffke (2011) has found that for a reduced frequency of $\kappa > 0.63$ the dynamic stall hysteresis curve of a Fulmar wing profile converges down onto a straight line. Figure 2.27 shows the experimental results using Particle Image Velocimetry (PIV) for the lift coefficient of this Fulmar-like profile. Figure 2.27 clearly shows that an increased reduced frequency closes the hysteresis curve. For the *LEO*-blade this would be equal to a frequency of 17.2 [Hz] at a resultant wind speed of 13.9 [m/s] and a chord length of 81 [mm]. These are values for the aerofoil within the oscillating flap closest to the root of the blade. This is also the aerofoil that is simulated using CFD in Section 2.5. The tested frequency range unfortunately only goes up to 13 [Hz] due to mechanical reasons. The stepper motor does not have enough power the oscillate the flap at a higher frequency.

Another key parameter for the dynamic stall behaviour is the amplitude of the oscillation. Past research by Schweickert (2016), Marchant (2017), Janssen (2018) and Neven (2020) have shown that an increase in amplitude directly increases the generated lift. The largest amplitude that was tested was 10 degrees for a total deflection of 20 degrees, starting from an AOA of 7 degrees. Hence the aerofoil oscillated between 7 and 27 degrees AOA. This amplitude also resulted in the largest generated lift. Unfortunately, the design of the flap mechanically limits the total increase in AOA. The change in AOA is determined by measuring the deflecting at the TE using a caliper. In the first set of experiments, the deflection of the TE is about 7 [mm]. This is equal to a change in AOA of approximately five degrees. This is the AOA of the entire aerofoil, the flap itself does make a larger change in angle.

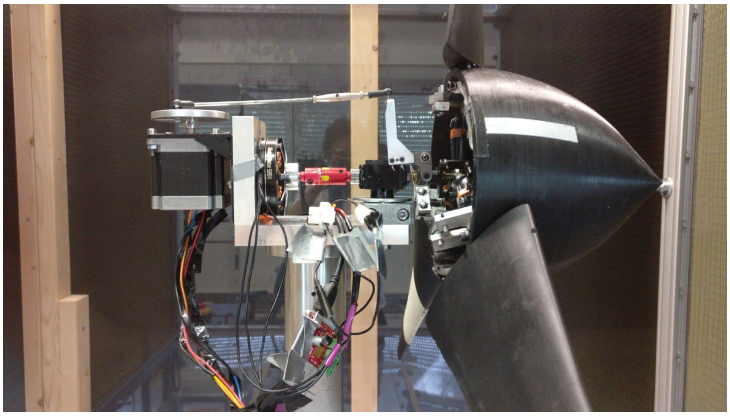

(a) Inside view

(b) Front view

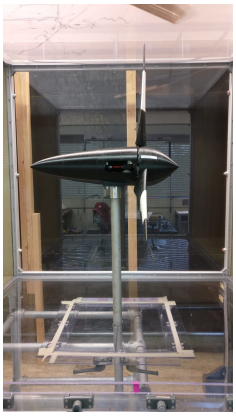

(c) Side view

Figures (2.28a-2.28c) show the experimental turbine inside the wind tunnel. Figure 2.28a clearly shows how the flaps are driven by the stepper motor. Interesting to see is also the pointy nosecone. CFD simulations have shown that, if the axis of the turbine is aligned with the wind flow, then a pointy nosecone creates a more attached flow compared to a rounded one.

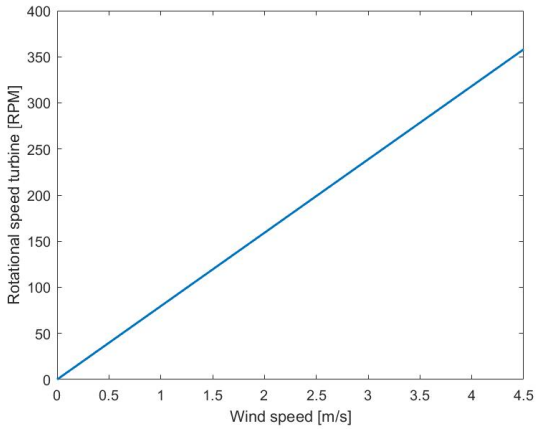

Figure 2.29: Rotational speed of the generator versus the wind speed.

Unfortunately, the second set of measurements were not able to indisputably prove the positive influence of the fast oscillating flap on the generated lift. This is because, even at the lowest load of one [Ω] which induces the highest current in the coils of the generator, the generator was spinning to fast. As a consequence, the angles of attack were very low. The reasons are explained in more detail in Section 3.1.
For this reason the test setup is changed in the third set of measurements. The delta configured load is removed and instead the phases of the generator are connected to a *Vesc six edu* speed controller board. The idea is that the speed controller board can set the speed of the generator, such that the correct TSR and the correct AOA are achieved. Using a fixed TSR, the speed of the generator is a function of just the wind speed. The range of rotational speeds as a function of the wind speed can be seen in Figure 2.29. The speed controller board is connected to a three-cell 11.4 [V] Li-ion battery, which supplies the required power. The speed controller produces a voltage and draws a current from the battery to rotate the generator at a fixed RPM. At close to zero wind speed, the generator is then run as a motor. Almost all of the required power is delivered by the battery. As the wind speed increases the power delivered by the battery should drop. At a certain wind speed, the delivered power by the battery pack should be zero. Up until this point a large size wind turbine would be idling. After this point, the power in the wind should be significant enough for the turbine to pick up speed. At this point the induced voltage by the speed controller should switch polarity and hence brake the generator. The interface of the speed controller logs the current and voltage input. When the flapping mechanism is turned on, the lift increases and as a consequence the power input by the speed controller should increase to compensate and keep the generator at a fixed speed. The measured values should not be seen as absolute values for increase in power generation. But the measured values for power with and without flapping can be compared with each other to determine if and with what percentage the generated power increases. To test this theory, the *Vesc* speed controller board is first connected to a *Turnigy D3530/15* AC generator which is connected to a battery powered drill. In specific the *Bosch GSR 12V-15* drill, which has a maximum rotational speed of 1300 [RPM] and a torque of 30 [Nm]. After this test the *Vesc* speed controller board is connected to the generator in the turbine and the tests are performed.

The results of the third test concluded that the generator was still not powerful enough. This will be elaborated in more detail in Section 3.1. For a forth test a final change to the turbine setup is made. The *Turnigy 5206 gimbal generator* is replaced with a *Turnigy SK8 6354-140kv sensored* brushless generator. This generator can handle currents up to 42 [A] and voltages up to 45 [V]. In addition to the generator being more powerful, it is also sensored which makes it more accurately controllable using the *Vesc speed controller* board.

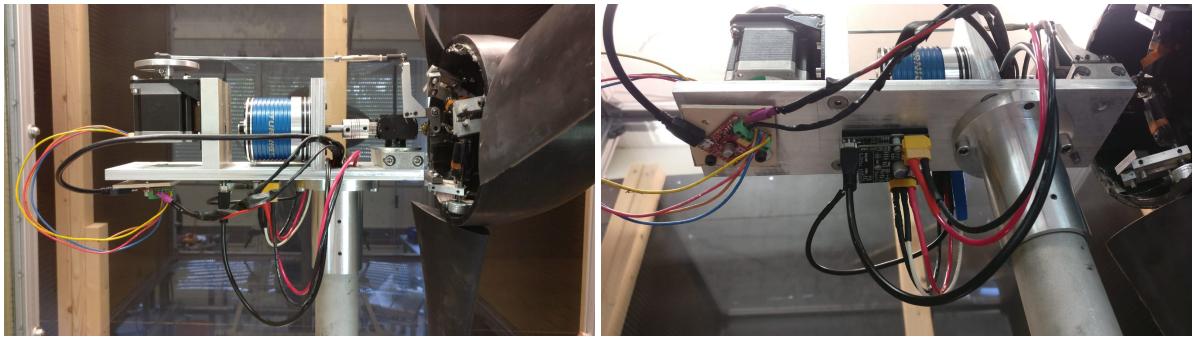

(a) Side view (b) Bottom view

Figure 2.30: Improved test setup including a new generator and a speed controller board.

To install the generator, the frame had to be remade as the new generator is too big for the original frame. The improved setup can be seen in Figures 2.30a and 2.30b. The generator is connected through a spring-type coupling to the axle of the rotor to accommodate for any misalignment.

(a) Zero/non-deflected flap (b) Maximum deflected flap

At this point, the experimental method is adjusted as well. As stated before, dynamic stall is a phenomenon caused by a sudden increase in angle of attack. However, for dynamic stall to have a noticeable influence the angle of attack must increase beyond the steady-state angle of attack at which the peak lift coefficient is achieved. Hence the exact angle of attack which corresponds to the peak of the lift curve must be determined before the influence of the frequency on dynamic stall can be tested. This is done by fixing the wind tunnel at a constant velocity and sweeping through an array of rotational speeds. The tested rotational speeds should correspond to a TSR range of 3.5 to 6 with a step size of 0.1. The turbine is run without oscillating the flap, using both a zero flap deflection and a maximum flap deflection. Figures 2.31a and 2.31b show the flap positions of zero deflection and maximum deflection respectively. Starting at a high TSR, the AOA along the span of the flap should be relatively small and hence the AOA should be in front of the peak. As a consequence, the maximum deflected flap should have a higher average power compared to the non-deflected flap. By decreasing TSR the AOA increase and the difference in lift between the two flap positions should decrease. This is because at some TSR the non-deflected flap is still in front of the peak, whilst the maximum deflected flap is beyond the peak. The TSR at which the difference in power output between the two flap deflections is the least is the optimal TSR to test the influence of the oscillation frequency on the dynamic stall.

$$c_p = \frac{P}{1/2 \rho A U_\infty^3} \tag{2.26}$$

To be able to compare the different wind speed and rotational speed cases the power output is divided by the total aerodynamic power in the wind to get the power coefficient as shown in equation 2.26.

2.5 CFD analysis

In this section the methodology of the CFD analysis is elaborated. The CFD analysis is divided into two parts. First 2D steady-state analyses of the aerofoil in the flap closest to the root of the blade are performed to determine the steady-state lift-coefficient versus AOA curve. This is needed as comparison for the dynamic curves to be able to determine whether the dynamic stall is achieved and if the dynamic stall increases the overall lift production. The results of these simulations are compared to the second set of dynamic analyses, which consist of the different oscillating trailing edge flap designs oscillating at different frequencies and different amplitudes.

The goal of the 2D analyses is to determine whether the length of the flap, in the direction of the chord, has a significant influence on the behaviour of the induced dynamic stall. This question arose during the design of the flap mechanism as stated in Section 2.2.

2.5.1 Initial and boundary conditions

Table 2.2: Free-stream parameters

Name	Value	Description
U_{inf}	13.8874 [m/s]	Free-stream velocity
ρ_{inf}	1.204 [kg/m^3]	Free-stream density
μ_{inf}	1.81410$\cdot^{-5}$ [kg/ m$\cdot$ s]	Free-stream dynamic viscocity
c	80.1 [mm]	Chord length
L	180$\cdot c$	Domain reference length
k_{inf}	0.1$\cdot \mu_{inf} \cdot U_{inf}/(\rho_{inf} \cdot L)$	Free-stream turbulent kinetic energy
ω_{inf}	10$\cdot U_{inf}$ / L	Free-stream specific dissipation rate
α	8	AOA

The CFD analyses are performed in Comsol Multiphysics version 6.0. All simulations follow the same model build, except for the dynamic simulations. The dynamic simulations have a few additional parameters to allow for the flapping motion in time. The model build starts with a list of free-stream parameters shown in table 2.2. These parameters correspond to a 2D aerofoil at 34%, or 15.3 [cm], of the blade radius. This aerofoil is chosen to analyse, as it located at the start of the flap and it has the most amount of play to increase or decrease the flap length in the chord-wise direction. Other important parameters are the fluid and solid materials. For the fluid the build in air properties are used. The flap is made from Ultimaker's TPU 95A. Hence the solid properties of the flap correspond to the material properties as listed by *UltiMaker*. The 3D printed TPU has a density of 1210 [kg/m^3], a young's modulus of 67 [MPa] and a poisson's ratio of 0.3897.

2.5.2 The geometry and its mesh

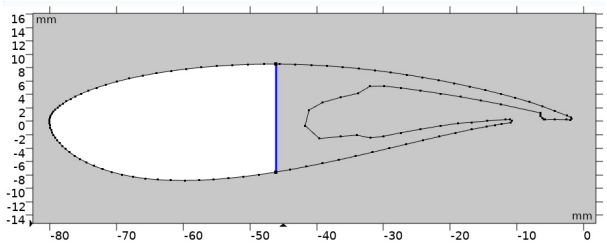

Figure 2.32: Mesh edge acting as fixed constraint.

As previously stated, the final study step requires solid mechanics physics to oscillate the flap. The longest flap that is analysed has a chord-wise length close to $\frac{1}{2}$C. To reduce the computational costs the aerofoil is divided into two parts with the division line at 0.42·C. The half of the aerofoil that is connected to the leading edge is solid and is modeled as a void in the fluid mesh. The second half, the flap, is flexible and is modeled as a solid mechanics physics hence requiring a mesh of its own. The division line between the two aerofoil halves acts as the fixed constraint for the solid mechanics. Figure 2.32 shows the mesh edge that acts as the fixed constraint.

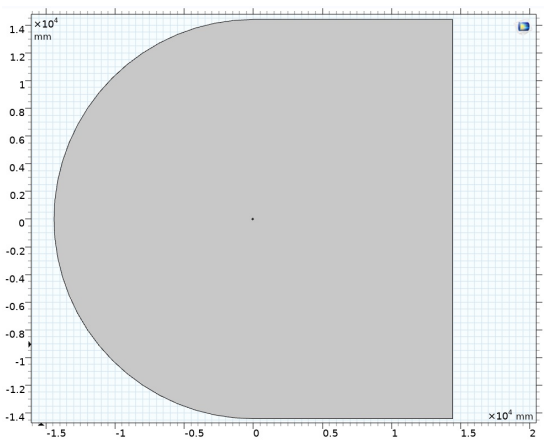

(a) Total flow field

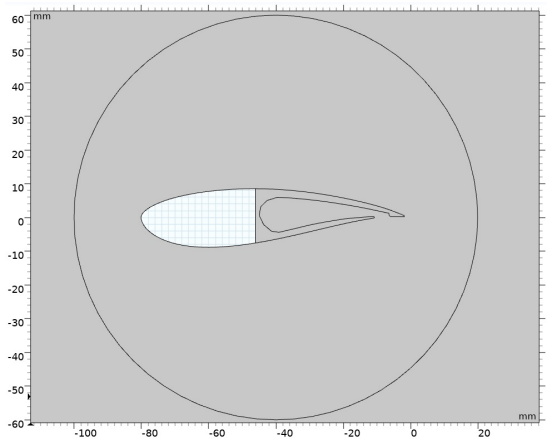

(b) Bigger flap and moving domain

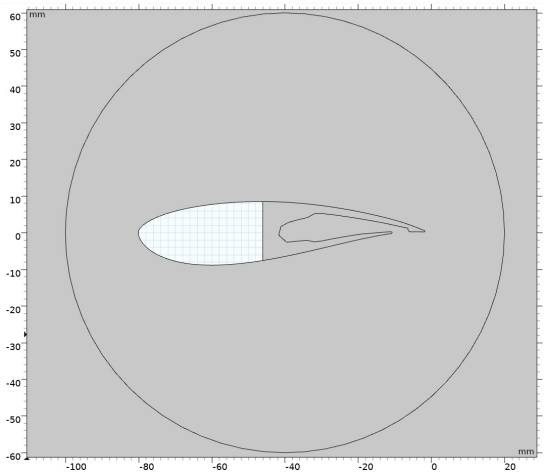

(c) Smaller flap and moving domain

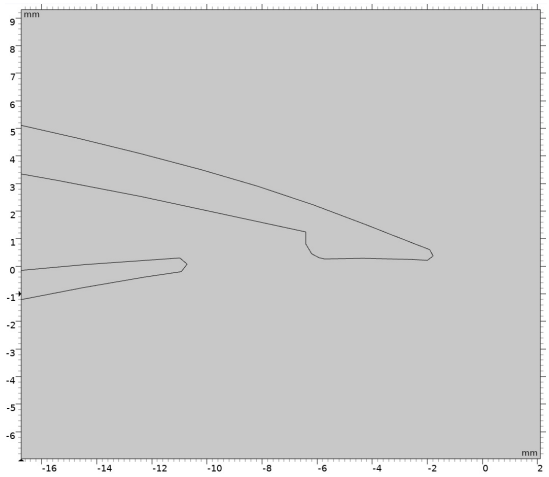

(d) Close-up on the TE

Figure 2.33: Simulated geometries

As explained in Section 2.2, in the real turbine the flap consists of a top and bottom part. The top part

is pushed down by means of a rotating arm. The top part then pushes on the bottom part which slides under the top part. This would not be feasible in the CFD simulation as the tiny mesh in between the two parts would collapse and invert resulting in a convergence error. To circumvent the convergence issue the gap between the two parts is enlarged and each part has its own prescribed displacement consisting of a maximum displacement in the y-direction and a waveform function depending of the frequency. Figures 2.33a and 2.33b show the total simulated flow field and the moving domain in combination with the aerofoil respectively. As stated before, the main reason for the CFD simulations is to determine whether the length of the flap in chord-wise direction has an influence on the dynamic stall behaviour. Hence a smaller flap, shown in Figure 2.33c, is also simulated. Figure 2.33d shows a close-up of the TE. As can be seen in the figure, the sharp point of the TE is rounded to decrease the computational cost and convergence issues.

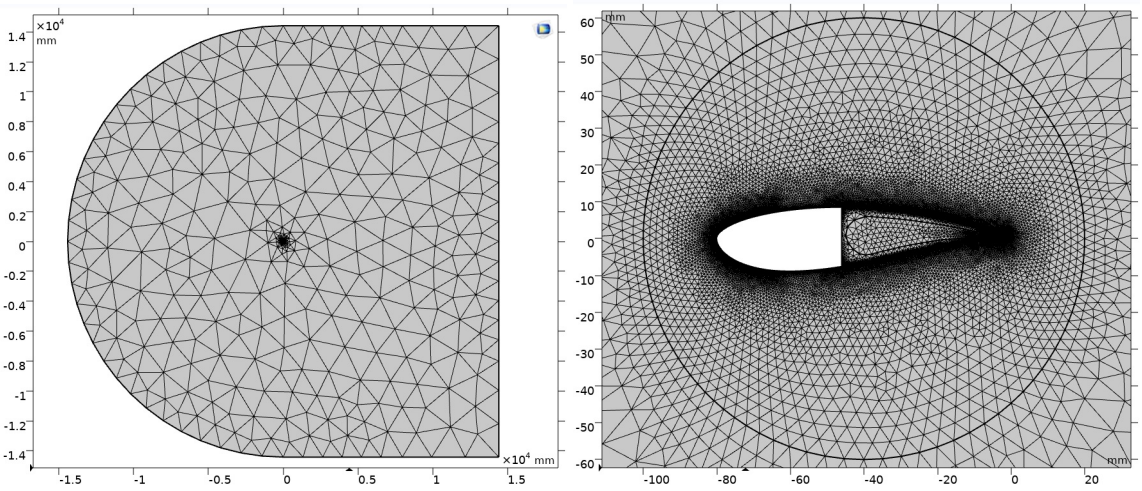

(a) Far field

(b) Moving domain with slightly larger flap

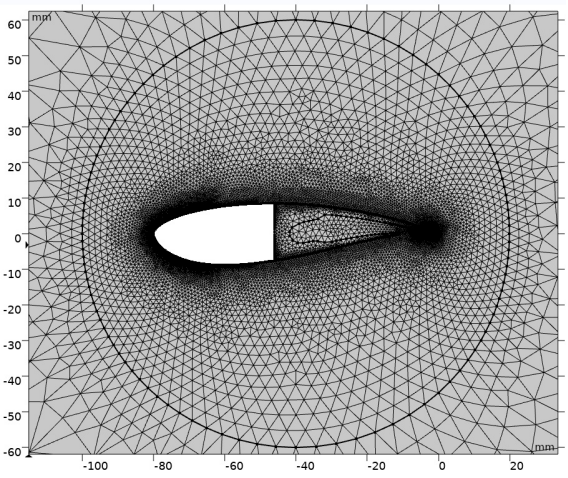

(c) Aerofoil with slightly smaller flap

Figure 2.34: Simulated meshes

The mesh starts coarse and is refined using the steady-state analyses. The mesh is refined until no significant change in lift is computed between two refinements. The refinement is limited as the computational cost for the dynamic simulations also needs to be considered. The leading and trailing edge of the finer mesh from Figure 2.34b have a very fine mesh in the order of 0.1 to 0.2 [mm] at the boundary layer. The size of the mesh gradually increases towards the middle of the aerofoil where it has a size of approximately 0.7 [mm].
The aerofoil is in the middle of a deforming domain enclosed by a circle with a radius of 60 [mm]. The

mesh size increases radially outward, away from the aerofoil, with a maximum of 1.1 times the previous mesh element resulting in a fine mesh as shown in Figure 2.34b. The far field mesh, as shown in Figure 2.34a, has an outwards increasing mesh size with a maximum of 1.8 times the previous mesh element.

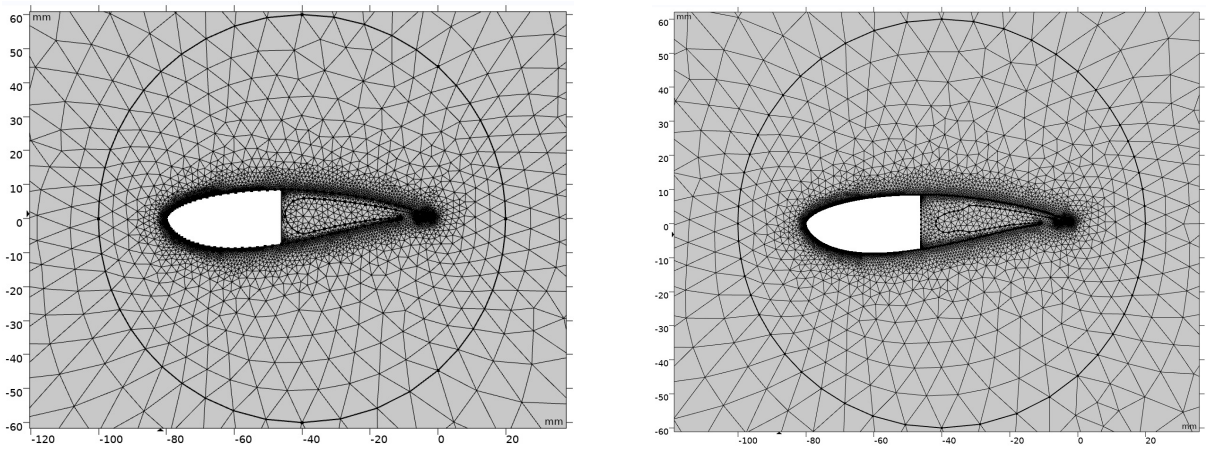

(a) Larger flap (b) Smaller flap

Figure 2.35: Coarser mesh of the moving domain

The mesh is also redefined during the dynamic simulations. First the mesh was refined at the boundary layer, as some simulations were not able to converge. Later the mesh was made coarser in radial direction to capture the influence on the hysteresis curves. The coarser mesh of Figure 2.35a has the same element sizes along the boundary layer as the finer mesh of Figure 2.34b, but the elements increase radially with a maximum of 1.25 times the previous element. The far field is kept the same. Figure 2.35b shows the coarser mesh for the smaller flap using the same parameters.

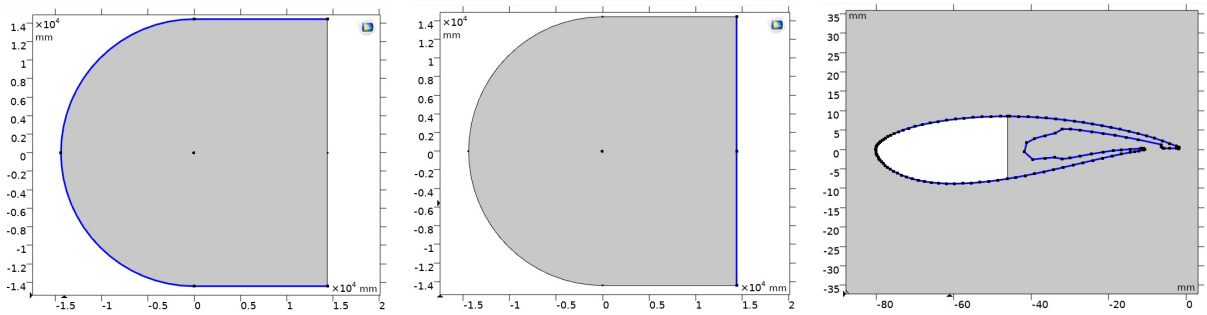

(a) Inlet (b) Outlet (open boundary) (c) No slip wall

Figure 2.36: Boundaries of the fluid flow

Since the CFD analyses should simulate an aerofoil in an open field fluid flow, the model requires an inlet, outlet and no walls other than the walls of the aerofoil. If there were other walls, the model would simulate an aerofoil inside a tube or on top of a plate, which would influence the results as these walls would have boundary layer effects on the flow. Figures 2.36a and 2.36b show the inlet and outlet of the fluid flow respectively. Figure 2.36c shows the wall at the surface of the aerofoil using a no slip boundary condition.

2.5.3 Study steps and solver models

The velocity field of the steady-state analyses is calculated in three steps and the field of the dynamic analyses is computed using four steps. First the potential flow is calculated using the Laplace classical

Partial Differential Equation (PDE). The calculated potential flow is an irrotational flow or in other words, a flow in which the curl or vorticity is zero everywhere. This is an incorrect assumption for the boundary layer and wake of the aerofoil, but it is acceptable for the far field of the fluid flow (Batchelor and Batchelor, 1967). In the second step the distance to the wall is calculated using the SST turbulence model. The SST turbulence model is used as it tends to be most accurate for flow near the wall of the aerofoil and hence more accurately computes the lift forces (Lyu, 2016). The wall distance initialisation step is used to reduce the computational cost by analytically computing the nonzero fluid velocity at the wall and in the viscous layer (Frei, 2017). The SST turbulence model combines the k-ω and k-ϵ turbulence models and interpolates between the two (Comsol, 2019b). In the near-wall region it uses the k-ω model and it switches to the k-ϵ model in the free shear flow.

$$\rho\frac{\partial k}{\partial t} + \rho\mathbf{u}\cdot\nabla k = P - \rho\beta_0^* k\omega + \nabla\cdot((\mu+\sigma_k\mu_T)\nabla k) \tag{2.27}$$

$$\rho\frac{\partial \omega}{\partial t} + \rho\mathbf{u}\cdot\nabla\omega = \frac{\rho\gamma}{\mu_T}P - \rho\beta\omega^2 + \nabla\cdot((\mu+\sigma_\omega\mu_T)\nabla\omega) + 2(1-f_{V1})\frac{\rho\sigma_{\omega 2}}{\omega}\nabla\omega\cdot\nabla k \tag{2.28}$$

Equations (2.27) and (2.28) show the equations derived from the k-ω model which solved analytically for the viscous layer(Comsol, 2019b). Where ρ is the fluid density, k is the turbulent kinetic energy, t is the time step, $\mathbf{u}$ is the fluid velocity, P is the production term, ω is the specific turbulence dissipation and μ_T is the turbulent or eddy viscosity. All other symbols are model constants. The SST turbulence model applies a no-slip boundary condition to the fluid at the wall, hence $\mathbf{u}$=0 at the wall. This also implies that k=0 at the wall and hence the SST model only solves for ω at the wall (Comsol, 2019b).

$$\rho\frac{\partial k}{\partial t} + \rho\mathbf{u}\cdot\nabla k = \nabla\cdot\left(\left(\mu+\frac{\mu_T}{\sigma_k}\right)\nabla k\right) + P_k - \rho\epsilon \tag{2.29}$$

$$\rho\frac{\partial \epsilon}{\partial t} + \rho\mathbf{u}\cdot\nabla\epsilon = \nabla\cdot\left(\left(\mu+\frac{\mu_T}{\sigma_\epsilon}\right)\nabla\epsilon\right) + C_{\epsilon 1}\frac{\epsilon}{k}P_k - C_{\epsilon 2}\rho\frac{\epsilon^2}{k} \tag{2.30}$$

Equations (2.29) and (2.30) show the transport equations used in the k-ϵ turbulence model (Comsol, 2019a). Equation (2.29) represents the turbulent kinetic energy and equation (2.30) represents the rate of dissipation of turbulent kinetic energy. Where P_k is again a production term, ϵ is the turbulent dissipation rate and all others are constants.

$$\lim_{l_w\to 0}\omega = \frac{6\mu}{\rho\beta_1 l_w^2} \tag{2.31}$$

Equation (2.31) shows the equation solved for ω at the wall, where the fluid velocity $\mathbf{u}$ and turbulent kinetic energy k are zero. In the far-field the fluid velocity $\mathbf{u}$ is not equal to zero and therefor the SST model has to set a boundary condition for both k and ω. Here l_w is the wall distance variable.

$$\frac{10^{-5}U_\infty^2}{Re_L} < k_\infty < \frac{0.1U_\infty^2}{Re_L} \tag{2.32}$$

$$\frac{U_\infty}{L} < \omega_\infty < 10\frac{U_\infty}{L} \tag{2.33}$$

Equations (2.32) and (2.33) show the boundary conditions for k and ω in the far-field respectively. U_∞ represents the far-field fluid velocity, L the approximate length of the computational domain and Re_L the Reynolds number of the computational domain.

In the third step the stationary velocity flow field is calculated using the SST turbulence model. For the steady-state lift-coefficient versus AOA curves a study extension is added in this step which sweeps over a whole range of angles of attack. For the dynamic simulations only the flow field at an AOA of five

degrees is computed. Later on this AOA is changed to eight degrees. The forth and final study step is only used for the dynamic simulations. This is a time-dependent study step in which the flow field is computed simultaneously with a moving solid. This requires a solid mechanics physics to move the flap, a moving mesh and a fluid-structure interaction to couple the fluid and structure physics. In this step, both step 2 and step 3 are continuously recomputed for each of the time steps.

Since the fluid as well as the solid mechanics are simulated in the final study step, a fully coupled solver is used to simulate the resulting fluid flow. The solver does have some difficulties to accurately simulate the fluid flow and hence a highly nonlinear solver method with a minimum damping factor of 1E-15 had to be used. The damping factor is the smallest time-step the solver is allowed to take. When there are large differences between adjacent vertices the solver will start taking smaller time-steps to reduce the error. This increases the computation time but allows more difficult models to still be solved.

From a physics perspective, the solid mechanics and fluid flow are coupled because the time-dependent result of one influences the input parameters of the other. As the solid mechanic deflects the flap, the change in geometry influences the fluid flow. But the change in fluid flow also influences the solid mechanics. For example, the fluid induces a stress in the flap. This could influence how the flap bends and this could again influence how the flow is deflected. From a maths perspective, the solid mechanics and fluid flow are fully coupled by forming a large single system of equations that solves for all of the unknowns(Comsol, 2023).

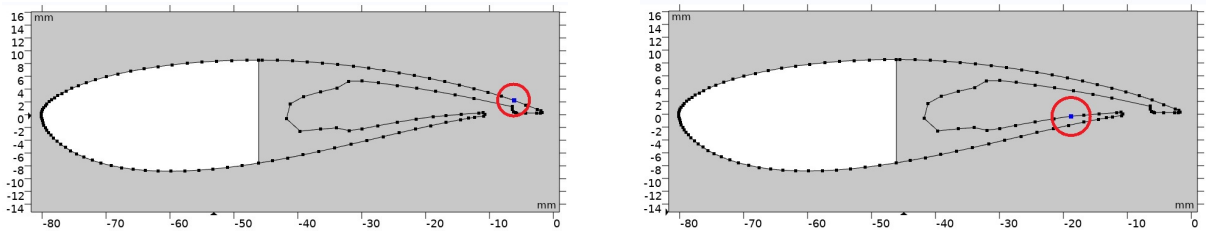

(a) LP side flap

(b) HP side flap

Figure 2.37: Vertices on which the prescribed displacements are added.

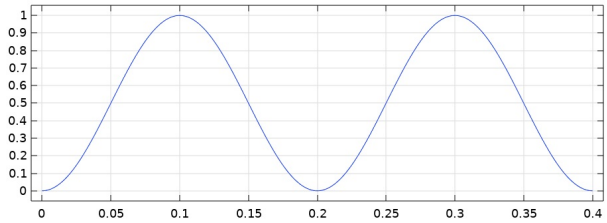

Figure 2.38: Example of the sinusoidal wave patterns used for the prescribed displacements.

To simulate the oscillatory motion, one prescribed displacement on the LP side and one prescribed displacement on the LP side are used. The displacement is purely in vertical direction. Though, due to bending of the material the vertices also experience a displacement in the horizontal direction. Figures 2.37a and 2.37b show the vertices on which the prescribed displacements are set.

Table 2.3: Values for maximum displacement of the respective vertex.

	LP side flap vertex	**HP side flap vertex**
Smaller flap	-7.73 [mm]	-4.6 [mm]
Bigger flap	-8.13 [mm]	-5.5 [mm]

The values of the displacement for the LP and HP side flap as well as for the smaller and bigger flap are not the same. The displacements follow a sinusoidal pattern as shown in Figure 2.38. The sinusoidal pattern is multiplied by the maximum displacement to get a time-dependent oscillatory motion of the flap. The phase of the sinusoidal pattern is shifted with $-1/2\pi$ to make the pattern start at zero amplitude. The period of the pattern is dependent on the simulated frequency where, for example, 10 [Hz] has a period of $1/10$. The values for the maximum displacements, in vertical direction, are shown in table 2.3. The values for the LP side displacement are chosen such that the change in AOA is about the same for the smaller and bigger flap. The values for the HP side deflection are chosen such that only a small gap is kept between the HP and LP side flap. This would simulate a flap moving underneath the TE. The gap is needed for the model to converge.

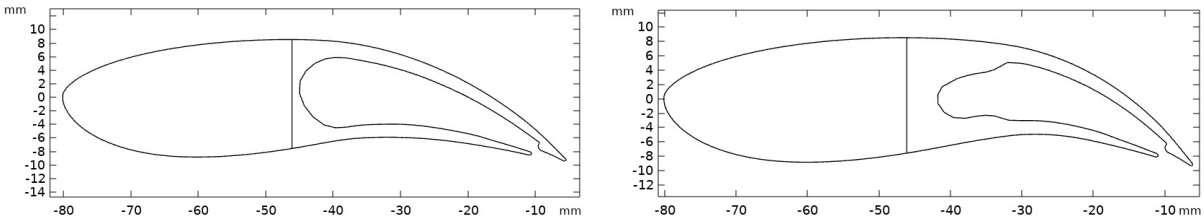

(a) Bigger flap

(b) Smaller flap

Figure 2.39: Deflection of the TE

Figures 2.39a and 2.39b show the maximum deflected positions of the bigger and smaller flap respectively. The increase in angles of attack due to the deflection of the TE for the bigger flap is approximately 7.19 degrees and for the smaller flap approximately 7.17 degrees.

2.5.4 Results analysis

CFD simulations are able to calculate parameters like pressure and velocity at each of the the vertices and interpolates the results over the surface of the triangular element. This is however, not the right format to compare the efficiency of aerofoils. The efficiency of an aerofoil depends on the total generated tangential force, which relies on the lift and drag forces. To be able to compare different aerofoils, the lift and drag coefficients need to be determined.

$$C_L = \frac{L}{1/2\rho U_\infty^2 c} \tag{2.34}$$

$$C_D = \frac{F_D}{1/2\rho U_\infty^2 c} \tag{2.35}$$

Equations (2.34) and (2.35) show the standard equations for the lift and drag coefficients respectively. For 2D aerofoils, the lift coefficient is a dimensionless value that relates the generated lift (L) to the dynamic pressure multiplied by the characteristic length (c). For aerofoils the characteristic length is the chord length. The dynamic pressure is equal to the kinetic energy divided by the area. The drag coefficient relates the drag force (F_D) to the dynamic pressure multiplied by a reference length. For 2D aerofoils the reference length is again equal to the chord length. Cousteix (2003) states that viscous forces are negligible compared to inertial forces for high Reynolds numbers flows, like around an aerofoil. The viscous forces do exist, but only in the boundary layer, which for an aerofoil is small. Hence, only the pressure forces are used in *Comsol Multiphysics 6.0* to compute the generated lift and drag.

$$C_L(\alpha) = \oint_c (c_p(s)/c)(n_y(s)\cos(\alpha)) - n_x(s)\sin(\alpha))ds \tag{2.36}$$

$$C_D(\alpha) = \oint_c (c_p(s)/c)(n_y(s)\sin(\alpha)) + n_x(s)\cos(\alpha))ds \tag{2.37}$$

$$C_p(s) = \frac{p(s) - p_\infty}{1/2\rho_\infty U_\infty^2} \tag{2.38}$$

Equations (2.36), reproduced from Comsol Multiphysics 6.0 (2021), and (2.37) show the relation between the pressure coefficient and the lift and drag coefficients respectively. The coefficients $n_y(s)$ and $n_x(s)$ relate to normal vectors in *y* and *x* direction of the mesh. Equation (2.38) shows the formula for the pressure coefficient, which relates the pressure difference created at a vertex (*p(s)* - p_∞) to the dynamic pressure of the free-stream fluid ($1/2\rho_\infty U_\infty^2$).

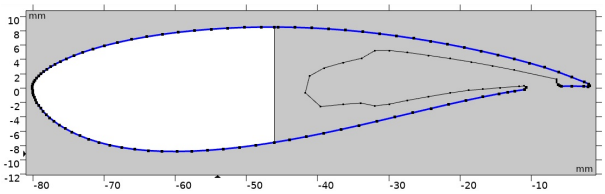

Figure 2.40: Boundaries over which the pressure is integrated

Figure 2.40 shows the area over which the pressure is integrated. The inside boundaries are neglected as they would not have an influence on the lift or drag on the real model.

The oscillating flaps are time-dependent analyses. The simulated pressure and velocity and the resulting lift and drag are simulated over a time domain. The simulated frequencies are 1, 5, 10, 15 and 20 [Hz]. For the frequencies of 10, 15 and 20 [Hz] a time frame of 0.5 [s] is simulated to get enough cycles. The 1 and 5 [Hz] frequencies are simulated for 1.1 [s]. This gives the 5 [Hz] frequency the same amount of cycles as the 10 [Hz] frequency. Due to time constraints, the 1 [Hz] frequency is only simulated for one cycle.

$$\frac{\alpha}{\delta t} = \alpha_{start} + \arctan\left(\frac{\delta y}{c - \delta x}\right) \tag{2.39}$$

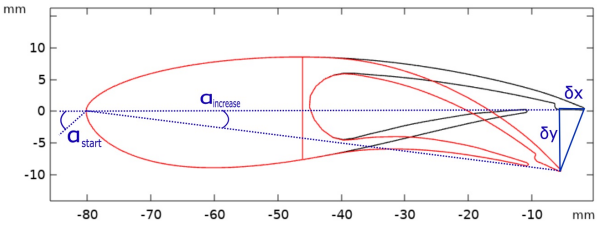

Figure 2.41: Change in AOA due to deflection of the TE.

To be able to compare the results of the time-dependent dynamic analyses to the steady-state values, the time domain is translated into an AOA domain. This is done by simulating the time-dependent deflection of the TE in both *x* and *y* direction. From this deflection a change in angle between the TE and the LE, a change in chord line, can be calculated. Adding this change in angle to the original AOA results in a time-dependent change in AOA as shown in equation (2.39). Figure 2.41 shows the change in AOA due to the deflection of the TE. The time-dependent lift and drag coefficients can then be plotted versus a time-dependent AOA, resulting in an AOA dependent lift and drag coefficient. If the model works as intended, the curve of the lift coefficient as function of AOA should look similar to the results of Noffke (2011) shown in Figure 2.27 as well as the CFD results from (Matz, 2010) and (Beil, 2016). Though

keep in mind that the results shown in Figure 2.27 are experimental results on a 3D model as opposed to CFD simulations on a 2D model.

3 Results

In this chapter the results of this research are elaborated. Section 3.1 presents the results gathered from the wind tunnel experiments and Section 3.2 elaborates on the results of the CFD analyses.

3.1 Wind tunnel experiments

To test the theory of increased lift due to dynamic stall induced by an oscillating flap the miniature wind turbine was placed into a wind tunnel. During the first measurement the oscillating flap was turned off and the blade pitch angle was set to zero degrees. Here, a blade pitch angle of zero degrees refers to the tip of the blade being perfectly in line with the plane of rotation. At first the turbine had some difficulties with starting up. This is because the centre of mass of the rotor was not perfectly aligned with the axis of rotation. At some point the wind speed was fast enough to produce a high enough pressure difference over the blade to overcome the resistance to turning.

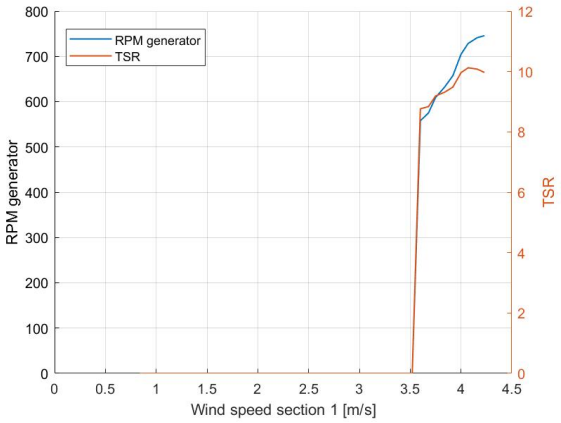

Figure 3.1: Results of the first measurement using 50 [Ω] resistors and a blade pitch angle of zero degrees.

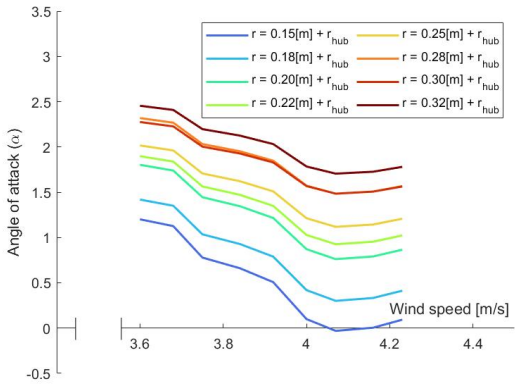

Figure 3.2: Angles of attack as function of the wind speed for various locations along the span of the flap.

Figure 3.1 shows the rotational speed of the turbine with respect to the wind speed. Figure 3.1 also shows the TSR achieved by the turbine. What is important to notice from this graph is that the TSR increases with the wind speed and it the value is higher than it should be. Large scale wind turbines aim to have a TSR of about 7 to 8 and the TSR should stay constant in the partial load region. Figure 3.2 shows the resulting angles of attack at various radii along the span op the blade. As can be seen from this figure the angles of attack are relatively low.

In an attempt to slow the turbine down and increase the angles of attack, the blade pitch angle was increased from zero to five degrees. In addition, the 50 [Ω] resistors were replaced with 1 [Ω] resistors to maximize the current flow. The larger the current through the generator the larger the braking force induced by the coils on the magnets of the rotor.

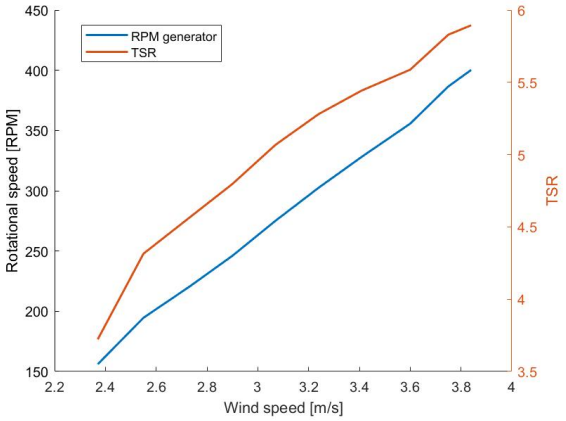

Figure 3.3: Results of the angular velocity measurements using 1 [Ω] resistors and a blade pitch angle of five degrees.

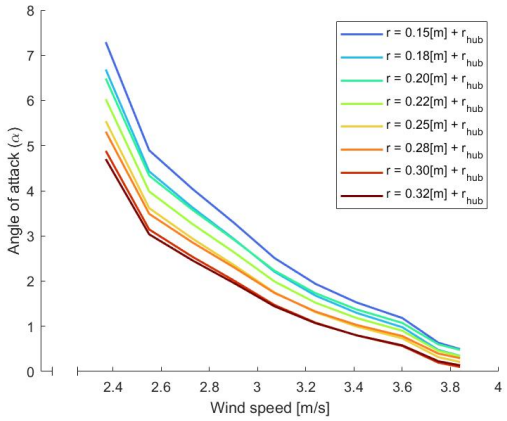

Figure 3.4: Angles of attack as function of the wind speed for various locations along the span of the flap.

Figure 3.3 shows again the angular speed of the turbine in RPM and the TSR. Figure 3.4 shows the resulting angles of attack for various locations along the span of the flap. Again the angles of attack are relatively low. After these measurements the first measurements with the oscillating flaps were performed. The flapping mechanism was tested at 10 and 1 [Hz]. The TE flaps and the driving mechanism designed during this thesis seemed to perform pretty well. The flaps were able to oscillate without tearing of the TPU or breaking of the driving mechanism.

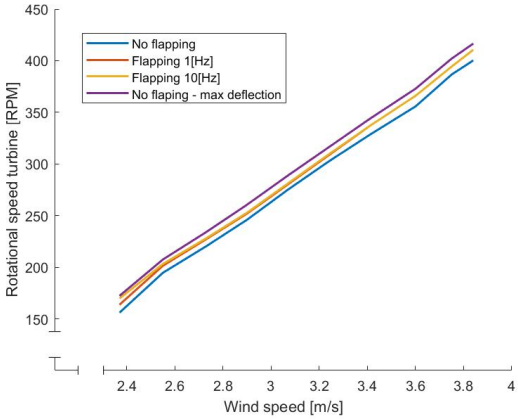

(a) Test 1/5

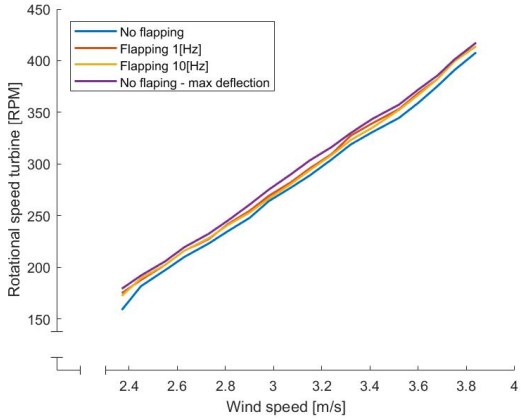

(b) Test 2/5

Figure 3.5: Angular velocity of the turbine as function of the wind speed for a static blade, oscillating flap at 1 [Hz], oscillating flap at 10 [Hz] and a static blade with maximum deflected flap.

Figure 3.5a shows the angular speed of the turbine as function of the wind speed for the static and flapping experiments. At first glance the flapping seems to be improving the generated lift on the blade. However, it should be noticed that the 1 and 10 [Hz] frequencies produced nearly identical results. This is because the angles of attack are so low, that the flapping motion is not able to push the blade into dynamic stall. In reality, the flapping motion is just increasing and decreasing the AOA along the steady-state curve. To test this, the flap was fixed in the maximum deflection position. If the flapping motion is indeed not inducing dynamic stall, then the lift produced by the maximum deflected flap should be more than the oscillating flap. Figure 3.2 shows the result of the maximum deflected flap and indeed a faster angular speed was measured. All of these tests were repeated five times to achieve statistical significance. Hence it was concluded that the current setup was not yet fully able to validate

the dynamic stall theory. It did however show that the oscillating flaps worked and were able to change the flow around the aerofoil, which is one of the main goals of this thesis.

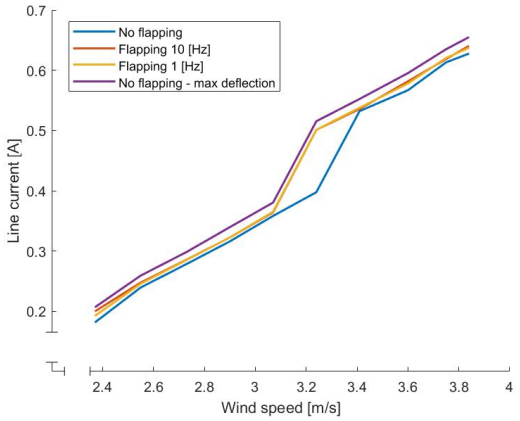

(a) Current

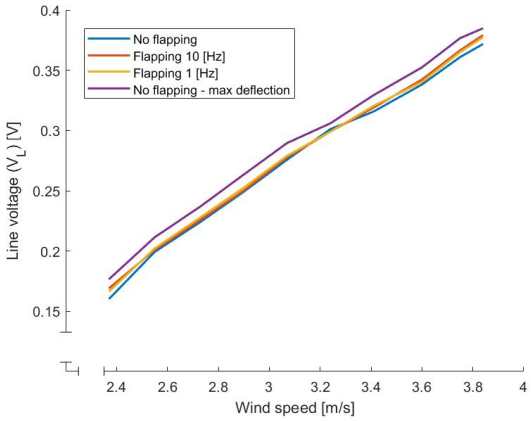

(b) Voltage

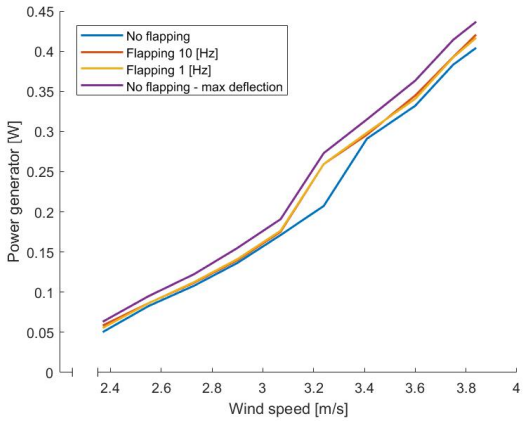

(c) Power

Figure 3.6: Measured results without flapping, flapping at 1 and 10 [Hz] and without flapping with the flap at maximum deflection.

Figures (3.6a-3.6c) show the measured values for the line current, phase voltage over the delta configured load and the calculated power in the *wye*-configured generator respectively. Each value is an average of 60 seconds with steps of one second. The figures again show the same pattern as figures 3.5a and 3.5b.

The main reason why this setup could not yet prove the theory is because the starting angles of attack, the angles of attack without flapping, were too low. The increase in AOA due to the flapping, which was about five degrees, was not able to push the AOA past the peak of the steady-state lift curve. The main reason why the angles of attack were too small is because the aerodynamic power of the rotor were in the order of 10 to 100 times larger compared to the generated electrical power at the generator. Hence only a small portion of the tangential force generated by the pressure difference is transformed into torque of the generator which produces electrical energy. The rest is transformed into angular velocity. The turbine speeds up and as a consequence the inflow angle and AOA decrease. The lower AOA generates a smaller pressure difference which generates a smaller tangential force until the tangential force is equal to the torque in the generator.

In a third test, the generator was driven by a *Vesc* speed controller board to control the speed and the resulting angles. First the *Vesc* speed controller board was tested on a separate generator to test if the speed controller board could deliver a steady rotational speed. The generator was connected to a drill to see if the generator, driven by the *Vesc* speed controller board, was able to slow the drill down to a

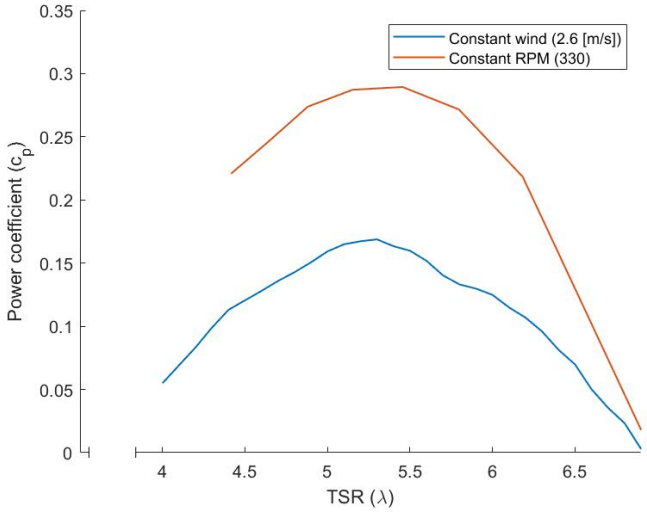

Figure 3.7: Power coefficient versus tip-speed-ratio for constant wind speed and constant rotational speed.

specific speed. A tachometer showed that the drill was free turning at 1000 [RPM]. The generator was able to slow it down by pushing 11 [A] of current through the generator at a voltage of 11.2 [V]. Hence it was considered that the board should work. However, after connecting the board to the generator in the turbine the board was not able to replicate the same results. This had two reasons. First of all, the generator is the turbine could not handle the high currents. At best the generator was able to handle about 0.6 [A]. Since torque is directly related to current, it was quite easy to stall the generator. Secondly, the *Vesc* speed controller board was advertised as a sensorless controller board, which determines the angle of the generator by the change in voltage. But since the generator could only produce low voltages, in the order of 1 [V], at relatively low rotational speeds, in the order of 500 [RPM], the speed controller was not able to accurately determine the angle of the generator. Hence, it was also not able to accurately send current to the generator to brake the turbine.

Figure 3.7 shows the power coefficient versus TSR for a constant wind speed of 2.6 [m/s] and a constant rotational speed of 330 [RPM]. These graphs are both for a non-deflected flap. Two important parameters should be noticed from Figure 3.7. First of all, since both graphs show the power coefficients of the same turbine the lines should overlap. However, the lower wind speed scenario of 2.6 [m/s] resulted in lower power coefficients. This is caused by more friction in the system at lower rotational speeds. For further research this friction should be limited by means that will be elaborated in the recommendations part of the discussion. Moreover, it should also be noted that the peak power coefficient is achieved at a TSR of about 5.3 to 5.5, which is lower than the design TSR of 7. This is most likely caused by a too aggressive twist angle. As shown in Section 2.1 the used twist distribution results in an approximate angle of attack of 5.5 along the full length of the blade. This is correct for larger turbines which have an optimum angle of attack closer to 6 degrees. However, due to the lower Reynolds numbers the optimum angle of attack for this turbine is actually closer to 10 degrees. This caused the peak power coefficient to shift towards a lower TSR. By lowering the twist distribution on a new design the angles of attack are increased and hence the peak should shift towards a TSR of 7. This should also result in a higher peak power coefficient and possibly a larger difference between flapping and not flapping.

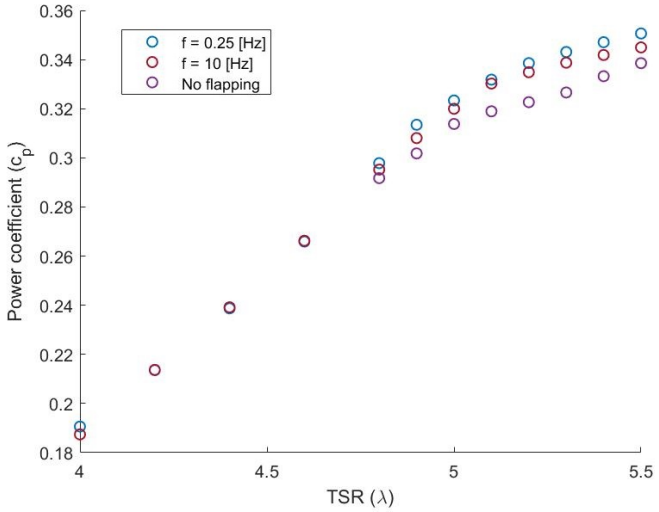

Figure 3.8: Power coefficient as function of TSR for flapping frequencies of 0.25 and 10 [Hz] and zero flap deflection.

Figure 3.8 shows the power coefficient as function of the TSR at a constant wind speed of 3.6 [m/s] for an oscillation frequency of 0.25 [Hz] and 10 [Hz]. For TSR larger than 4.8 also the power coefficient for a non-deflected flap are shown. Figure 3.8 shows that for all tested TSR above 4.8 the c_p of both 0.25 and 10 [Hz] are above the non-deflected flap. Hence, for these TSRs the AOA is too small to test the dynamic stall. Figure 3.8 also shows that for a TSR of 4 and a TSR above 4.8 the power output of the 0.25 [Hz] oscillating flap is larger than the 10 [Hz] oscillating flap, whilst for a TSR between 4.2 and 4.6 the values are similar. The difference between the lower and higher frequencies can again be explained by friction in the system. During the oscillation cycle, a part of the force is used to compress the spring coupling. This is unwanted behaviour and should be addressed in a new design. The amount of compression depends on the wobbling of the nosecone, another unwanted behaviour which should also be addressed in a new design. At the slower oscillation frequency the coupling is able to fully decompress at the end of the cycle, whilst for the higher frequency the coupling is still partly compressed at the end of the cycle. Hence, the amount of deflection at higher frequencies is lower compared to the lower frequency.

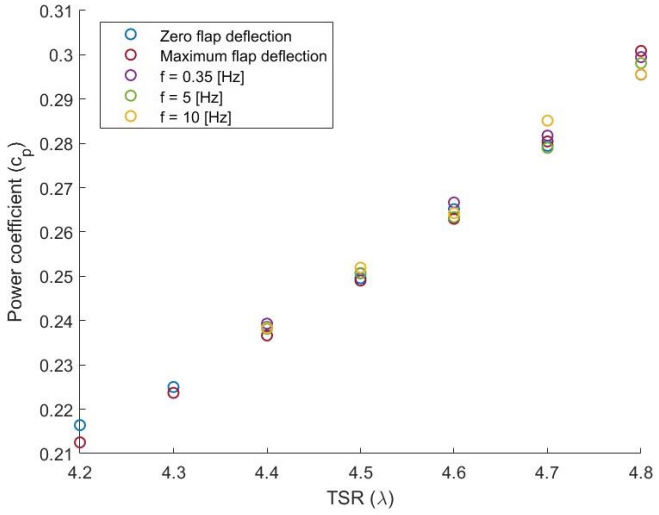

Figure 3.9: C_p as function of TSR for zero flap deflection, max flap deflection and oscillation frequencies of 0.25, 5 and 10 [Hz].

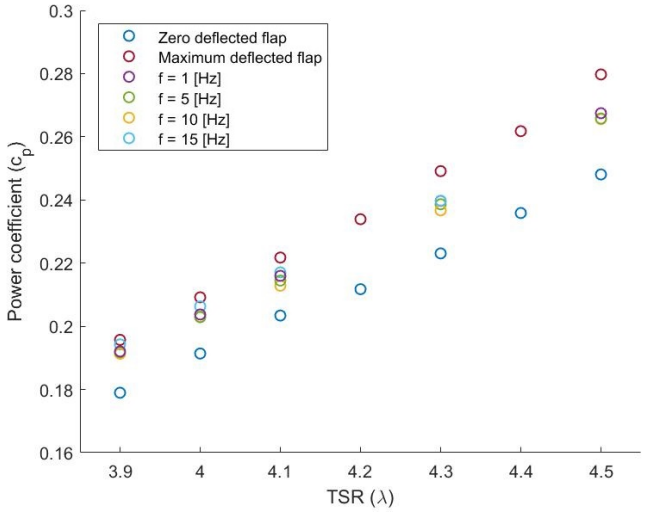

Figure 3.10: C_p as function of TSR for zero and maximum flap deflection and for oscillation frequencies of 1, 5, 10 and 15 [Hz].

Figure 3.9 shows again the c_p as function of the TSR in the range of 4.2 to 4.8 at a wind speed of 3.6 [m/s]. The plotted results are for a zero flap deflection, a maximum flap deflection and for oscillation frequencies of 0.25, 5 and 10 [Hz]. Since the difference in power coefficients for zero and maximum deflected flaps is small, this is most likely the range of TSR at which the angle of attack along the span of the flap is close to the peak. Figure 3.9 does show some differences between the different oscillation frequencies. However, the differences are not consistent between the tested TSRs. Moreover, the difference in c_p compared to the zero flap deflection, less than 1%, is not enough to be considered significant.

Figure 3.10 shows the c_p as function of the TSR for a wind speed of 4.2 [m/s]. This experiment started with a TSR of 4.5 and went down to a TSR of 3.9. Again the power coefficient for the maximum deflected flap is higher compared to zero flap deflection and the oscillating flap is in between. Hence, for these TSRs at this wind speed the AOA is again too low to test dynamic stall. Unfortunately, due to time scheduling of the wind tunnel, time ran out to perform additional experiments after the measurements at a TSR of 3.9.

3.2 CFD analysis of the oscillating flap

In the first step of the CFD analyses the mesh is refined by simulating the steady-state lift curves. Figure 3.11 shows the resulting lift curves for the refined meshes. As can be seen from the curves, the finer meshes that were simulated do not exactly converge to a single line. Refining the mesh even further could have done that, but it would significantly increase the computational cost.
There are two important things to notice from the graph. First of all, the peak of the lift curve decreases with an increase in refinement from number 3 to 5 but increases again with number 6. The peaks of 4 and 6 are relatively close together and since the coarser mesh number 4 requires a little less computational effort compared to mesh number 6, the decision was made to use mesh number 4 for the dynamic simulations.

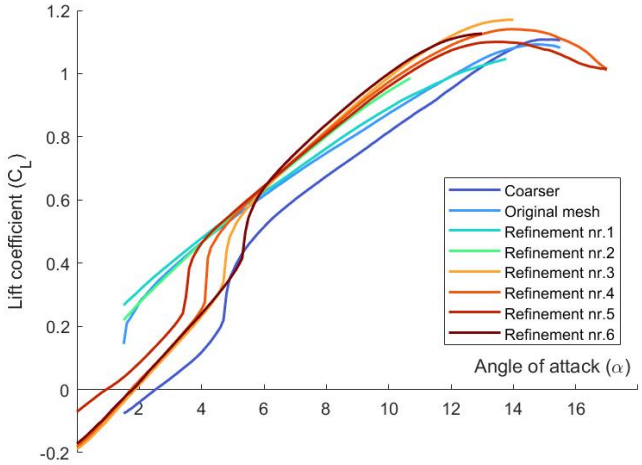

Figure 3.11: Steady-state mesh refinement analysis

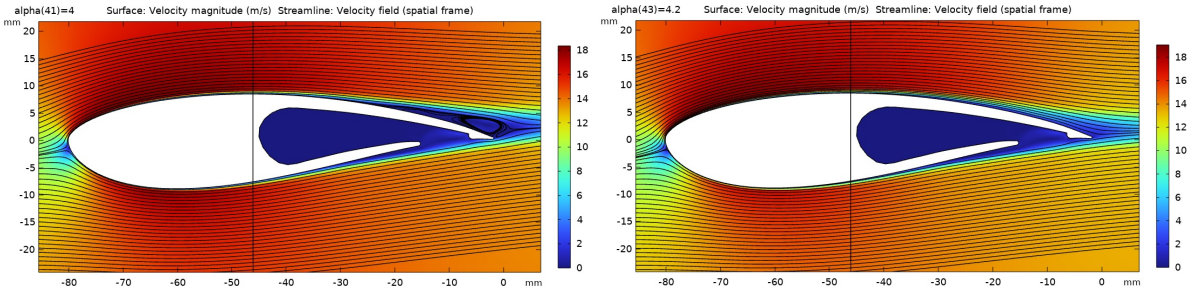

(a) AOA = 4 degrees

(b) AOA = 4.2 degrees

Figure 3.12: Steady-state velocity field around the *NREL S835* aerofoil.

The second thing to notice is the step-wise increase in the lift coefficient at about three to five degrees AOA depending on the mesh. This step does not exist in reality and it is purely an effect of the simulation. Figures 3.12a and 3.12b show the velocity flow fields at 4 and 4.2 degrees AOA respectively. Figure 3.12a shows a small vortex at the TE which has disappeared in Figure 3.12b. This vortex is the main cause for the step-wise increase in the lift coefficient and it is likely caused by an instability in the boundary layer due to the design of the mesh. During the dynamic simulations, the mesh was refined once again and the step was gone. To be absolutely certain of this, a mesh refinement study could have been done. However, due to time constraints this was considered to be outside of the scope.

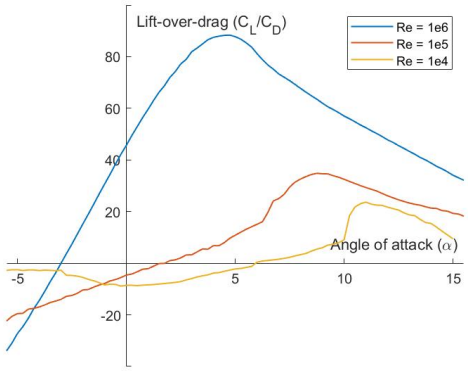

(a) NREL S835 aerofoil

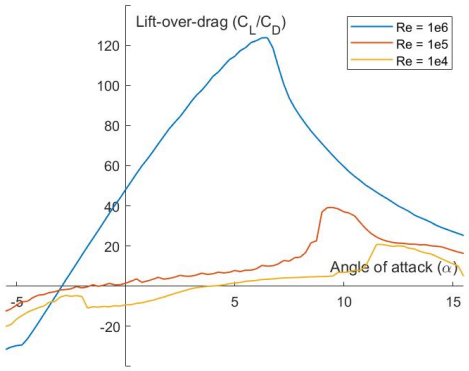

(b) NACA 64-418 aerofoil

Figure 3.13: Lift-over-drag curves as function of AOA at different Reynolds numbers (data points reproduced from Airfoil Tools (2023)).

As shown in Figure 2.2b in Section 2.1 the average AOA along the span of a blade with a TSR of 7 is about five degrees. Hence, the first dynamic simulations used a starting AOA of five degrees. However, this starting angle was later changed to eight degrees as the maximum AOA due to the TE deflection was not able to go beyond the peak of the lift curve. The simulated deflection increases the AOA with about seven degrees. This would result in a maximum AOA of 12 degrees, whilst the peak of the lift curve, as shown in Figure 3.11, is at about 14 degrees. Figures 3.13a and 3.13b show the lift-over-drag curves for the NREL S835 and NACA 64-418 aerofoils generated using *XFOIL*. These figures show that for larger turbines the ideal AOA is indeed close to five to seven degrees, but for smaller turbines, like the experimental setup, the ideal AOA shifts towards eight to twelve degrees.

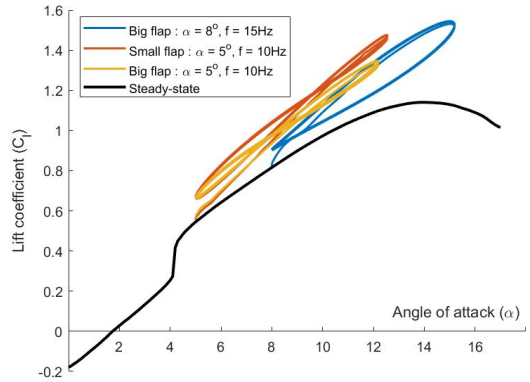

Figure 3.14: Results of the big and small flap simulations using the original mesh at oscillation frequencies of 10 and 15 [Hz].

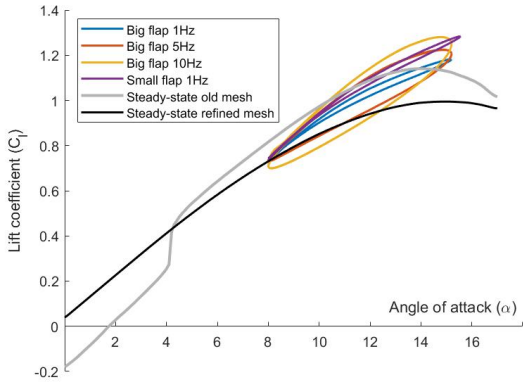

Figure 3.15: Results of the big and small flap simulations using finer mesh at oscillation frequencies of 1, 5 and 10 [Hz].

Figures 3.14 and 3.15 show the first results of the CFD analyses on the effect of the flap length. Figure 3.14 shows the first set of simulations using the refined mesh number 4. The figure shows the result in lift coefficient for the bigger and smaller flap starting at an AOA of five degrees and oscillating at a frequency of 10 [Hz]. In addition, also the resulting lift coefficient for the bigger flap starting at an AOA of eight degrees and an oscillation frequency of 15 [Hz] is shown. The results are compared to the steady-state curve. The figure shows that the length of the flap does have an influence on the resulting lift, where the smaller flap results in a higher lift coefficient.

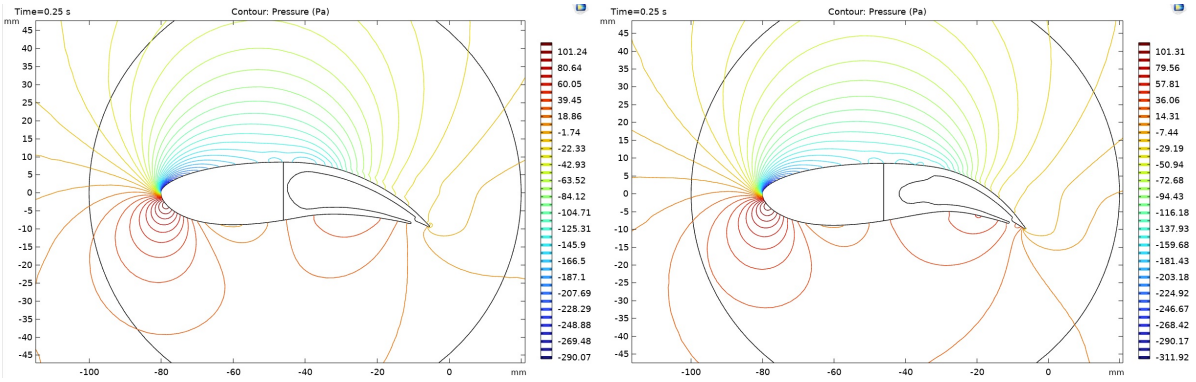

(a) Bigger flap (b) Smaller flap

Figure 3.16: Pressure fields of the *NREL S835* aerofoil with a bigger and a smaller flap at maximum deflection and a staring AOA of five degrees.

The difference in resulting lift could be explained by the fact that, even though the total aerofoil has the same change in AOA, the angle of the flap itself is a lot steeper for the smaller flap. As a consequence, the vertical component of the velocity field at the TE is larger for the smaller flap and hence the pressure difference shown in Figures 3.16a and 3.16b is different. Important to notice in Figure 3.14 is again a step-wise increase in the lift coefficient. This is most likely caused by a too coarse mesh at the boundary layer.

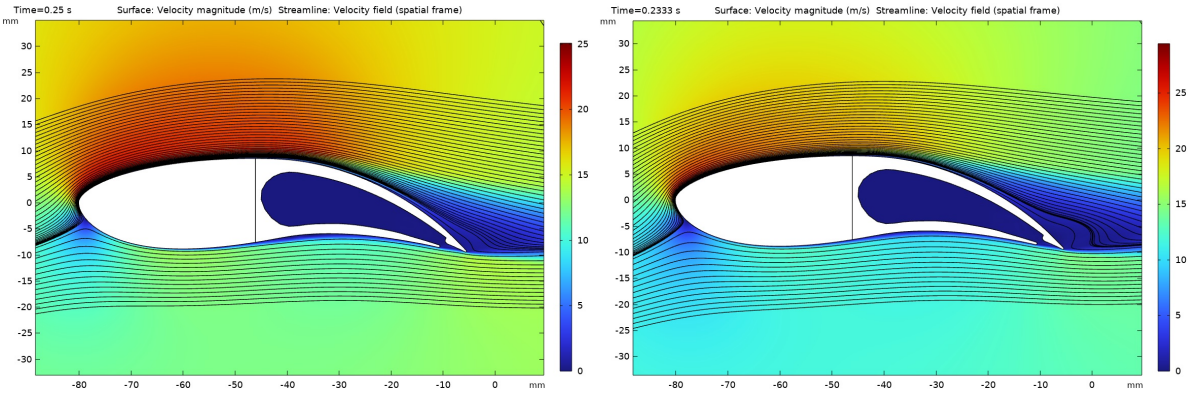

(a) Starting AOA five degrees. (b) Starting AOA eight degrees.

Figure 3.17: Velocity fields around the *NREL S835* aerofoil using the bigger flap at maximum deflection.

Figures 3.17a and 3.17b show the velocity fields around the maximum deflected bigger flap using a starting AOA of five and eight degrees respectively. Important to notice from these figures is the absence of a vortex. Which is inherently inconsistent with the theory of dynamic stall as it requires a vortex to function. The absence of a vortex is again most likely caused by a too coarse mesh at the surface of the aerofoil. For this reason the mesh is refined at the boundary layer. Moreover, due to reasons explained before the AOA is changed to eight degrees for all other simulations. Figure 3.15 shows the results of the bigger flap, using the refined mesh, simulated at an oscillation frequency of 1, 5 and 10 [Hz] as well as the smaller flap simulated at a frequency of 1 [Hz]. Important to realize from Figure 3.15 is that the 1 [Hz] simulations seem to follow a narrower loop compared to the 5 and 10 [Hz] simulations. In addition, the 5 [Hz] simulation also follows a narrower loop compared to the 10 [Hz]. This would suggest that lower oscillation frequencies would result in a more efficient blade, which contradicts all of the research done before. Averaging the lift coefficients resulted in an average lift coefficient of 0.9835 for the 1 [Hz] loop, 0.9892 for the 5 [Hz] loop and 0.989 for the 10 [Hz] loop. However, it does seem to be more accurate compared to the first mesh. The steady-state curve no longer has a step-wise increase at four

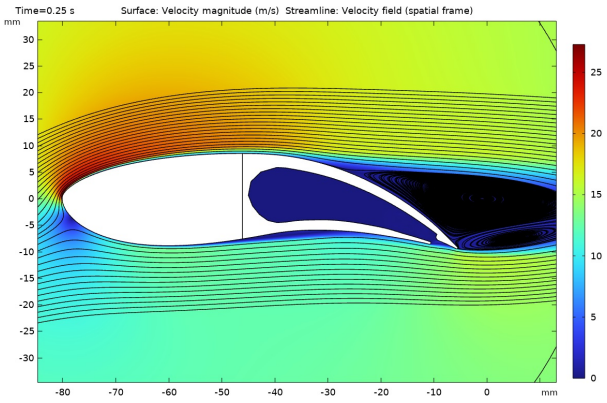

Figure 3.18: Velocity field around the *NREL S835* aerofoil using a bigger flap at maximum deflection and a starting AOA of eight degrees, showing a large vortex at the flap.

degrees AOA and the dynamic curves are more in-line with the steady-state curve. Moreover, this mesh is able to generate a vortex as can be seen in Figure 3.18.

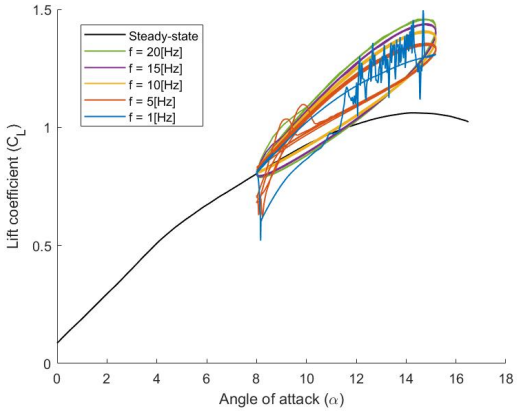

(a) Lift coefficient as function of the AOA

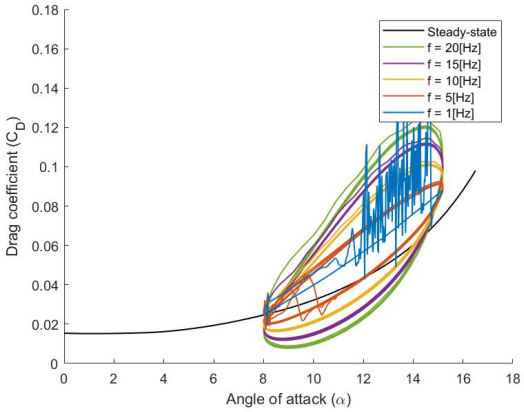

(b) Drag coeff. as function of the AOA

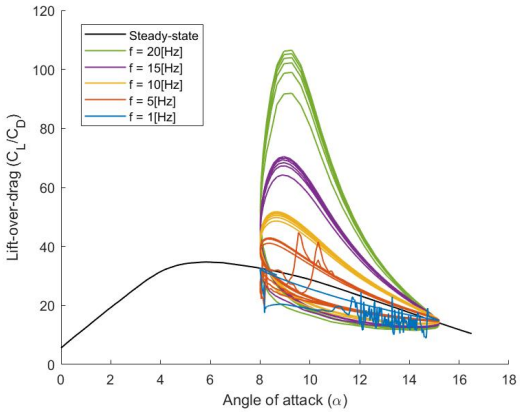

(c) Lift-over-drag as function of the AOA

Figure 3.19: CFD results of the bigger flap for the oscillation frequencies of 1, 5, 10, 15 and 20 [Hz].

According to the dynamic stall theory, slower frequencies should suffer from large hysteresis curves. In order to get these hysteresis curves appear in the simulations, the mesh is made coarser in radial direction. The mesh at the surface of the aerofoil was kept the same. This keeps the mesh fine at the boundary layer, but makes it more coarse in the flow field around the aerofoil. The resulting mesh was

shown in Figure 2.35a in Section 2.5.2. Figures (3.19a-3.19c) show the lift coefficient, drag coefficient and lift-over-drag as function of the AOA. The shown results are from the 1, 5, 10, 15 and 20 [Hz] oscillation frequencies for the bigger flap. Figure 3.19a shows that, due to the oscillating flap, the lift coefficient increases beyond the peak of the steady-state curve. Figures 3.19a and 3.19b show that the 1 [Hz] oscillation frequency shows significant hysteresis and the 5 [Hz] frequency shows some hysteresis, whilst the others show no hysteresis. Figures 3.19a and 3.19b also show that the lift and drag coefficients reach higher values for higher oscillation frequencies. In Figure 3.19c the lift is divided by the drag to get the lift-over-drag ratio. This ratio shows a clear increase in value for higher frequencies.

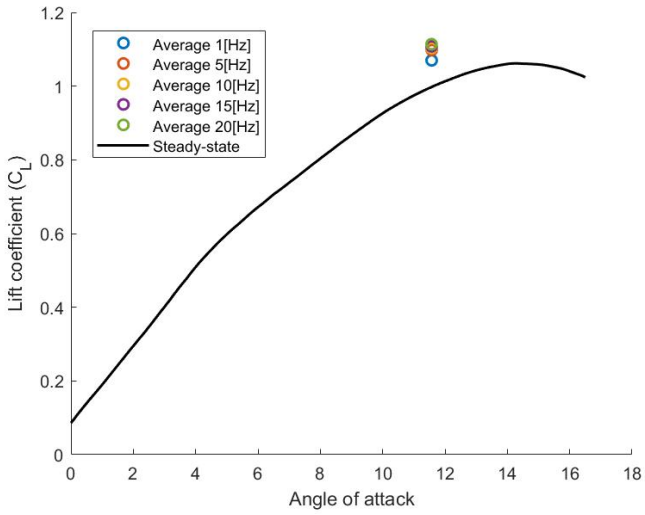

Figure 3.20: Average lift coefficients throughout the oscillation cycles.

Figure 3.20 shows the average lift coefficients throughout the oscillation cycles at the average AOA. The values are compared to the steady-state curve of the same mesh. Important to notice is that even though the 1 [Hz] frequency experiences some hysteresis, the average lift is still more compared to the steady-state line. An explanation for this could be that 3D effects play a key role in the dynamic stall behaviour. The simulations are performed using the SST RANS turbulence model, which is very accurate for steady-state analyses but could oversimplify dynamic simulations. Large Eddy Simulations (LES) could more accurately compute dynamic simulations. Unfortunately, *Comsol Multiphysics 6.0* does not offer LES for 2D simulations. Nevertheless, even though the SST turbulence model is less capable of simulating the dynamic behaviour, we can still see a difference between the lower and higher oscillation frequencies. Moreover, the main goal of the CFD analyses is to determine if the length of the flap has an influence on the generated lift. This can still be analyzed.

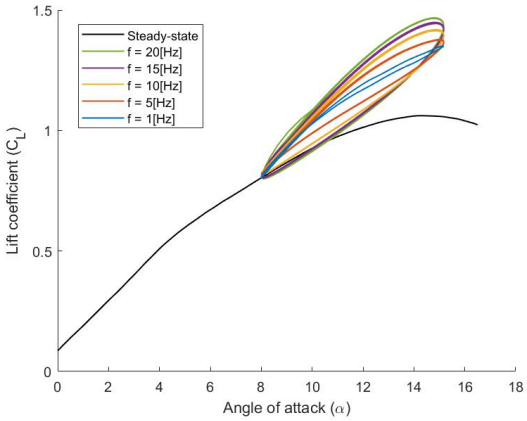

(a) Lift coefficient as function of the AOA

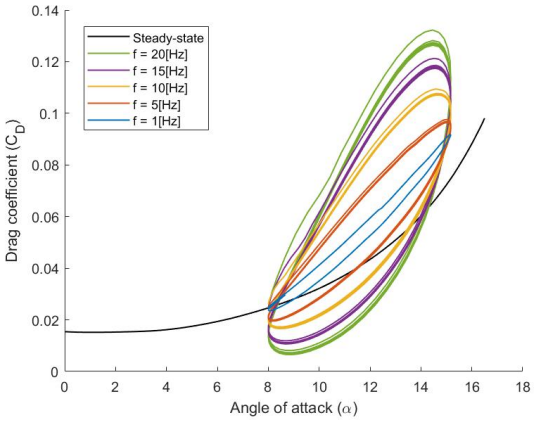

(b) Drag coefficient as function of the AOA

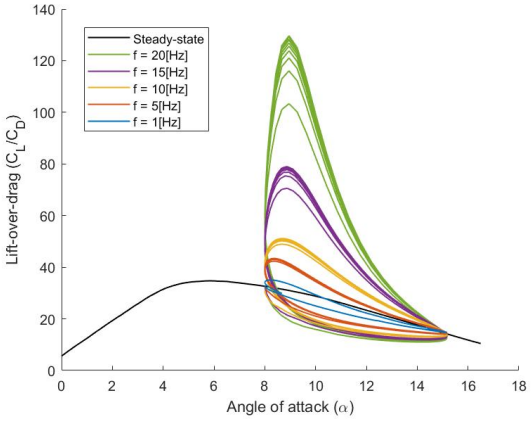

(c) Lift-over-drag as function of the AOA

Figure 3.21: CFD results of the smaller flap for the oscillation frequencies of 1, 5, 10, 15 and 20 [Hz].

Figures (3.21a-3.21c) show again the lift coefficient, drag coefficient and lift-over-drag ratio as function of the AOA respectively. The shown results are from the 1, 5, 10, 15 and 20 [Hz] oscillation frequencies for the smaller flap. The same conclusion can be drawn as for the bigger flap: an increase in frequency results in an increase in lift performance. Important to notice, however, is the absence of stalling hysteresis at the 1 [Hz] frequency. This is most likely due to the solver settings rather than a representation of reality.

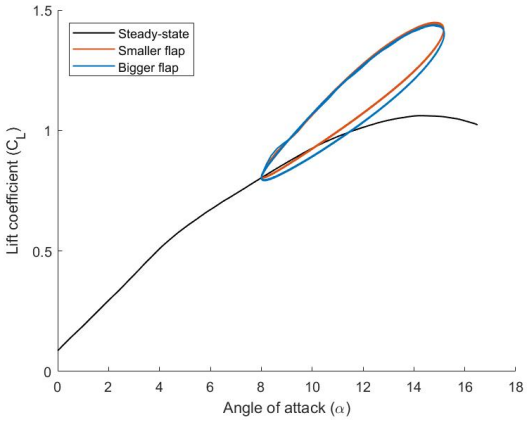

(a) Lift coefficient as function of the AOA.

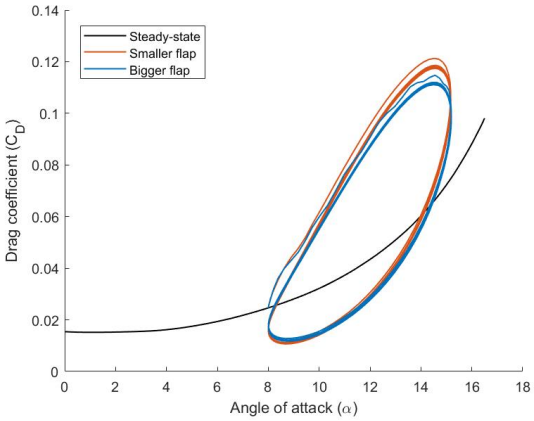

(b) Drag coefficient as function of the AOA.

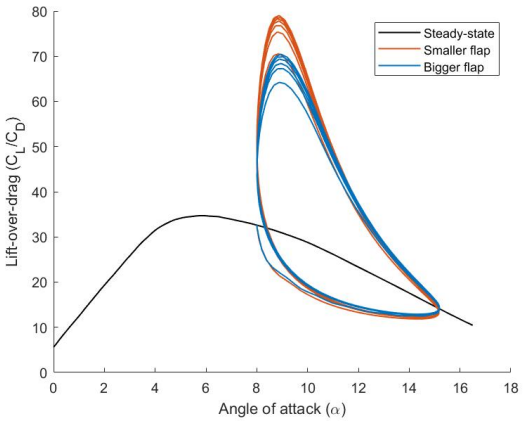

(c) Lift-over-drag as function of the AOA.

Figure 3.22: Comparison between the bigger and smaller flap for an oscillation frequency of 15 [Hz]

Table 3.1: Averaged lift, drag and lift-over-drag for the bigger and smaller flap at various oscillation frequencies.

	Average Cl	**Average Cd**	**Average Cl/Cd**
Bigger flap			
1 [Hz]	1.0699	0.0588	20.3960
5 [Hz]	1.0981	0.0544	23.6341
10 [Hz]	1.1035	0.0541	26.7616
15 [Hz]	1.1077	0.0552	30.3215
20 [Hz]	1.1138	0.0562	36.2233
Smaller flap			
1 [Hz]	1.1140	0.0545	23.4326
5 [Hz]	1.1188	0.0558	24.4085
10 [Hz]	1.1184	0.0572	26.0328
15 [Hz]	1.1284	0.0587	30.6705
20 [Hz]	1.1297	0.0583	39.3010

Figures (3.22a-3.22c) show again the lift coefficient, drag coefficient and lift-over-drag ratio as function of the AOA. The shown results compare the smaller and bigger flap at an oscillation frequency of 15

[Hz]. The results show again that the smaller flap increases the overall lift coefficient. Table 3.1 shows the lift, drag and lift-over-drag values averaged over a full oscillation cycle for each of the simulations. At 15 [Hz] the lift coefficient increased from 1.1077 for the bigger flap to 1.1284 for the smaller flap, whilst the length of the flap decreased from 0.507·C to 0.6·C. This is a percentile increase in lift of 1.87% for a change in length of 0.093·C. Therefore it can be concluded that, as long as the change in AOA is kept the same, a design with a smaller flap would be preferred to a design with a bigger flap. A smaller flap, however, would induce higher stresses and is thus more prone to fatigue.

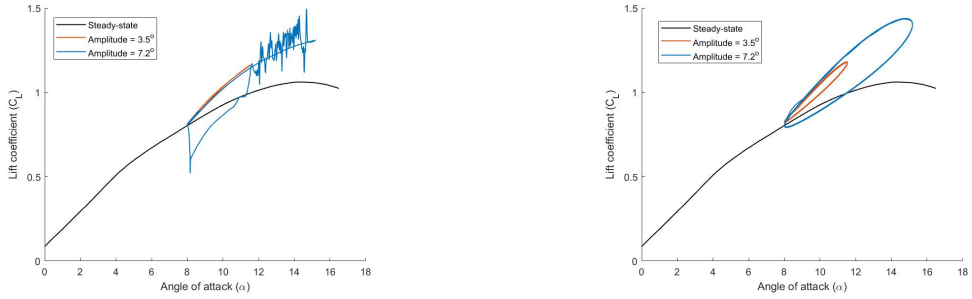

(a) 1 [Hz] oscillation frequency

(b) 15 [Hz] oscillation frequency

Figure 3.23: Lift coefficient as function of the AOA for a larger and a smaller amplitude.

Figure 3.23a and 3.23b show the lift coefficient for the bigger flap for the oscillation frequencies of 1 and 15 [Hz]. The curves are compared to the same oscillation frequencies with a lower amplitude of 3.5 degrees. The figure shows that a lower amplitude directly influences the generated lift. This is as expected, as a lower amplitude directly relates to a smaller change in AOA. Another important aspect to notice is the relatively straight line for lower amplitude the one Herz frequency. As the smaller amplitude only goes up to an AOA of about 11.5 it does not go beyond the peak of the steady-state curve. Hence it should not yet encounter dynamic stall and it could be that this line is a more accurate representation of the steady-state curve.

4 Discussion

This report has presented a working experimental scale wind turbine model with oscillating TE flaps. However, the experimental results should be interpreted carefully as there were some limitations to the research. This chapter reflects on the research process, by discussing the limitations as well as the implications for the interpretation of the results. The chapter ends with some recommendations.

In Chapter 2 the methodology of this research is elaborated. Section 2.1 the design of the blade is verified and adjusted where needed. The calculations show that the twist of the blade was designed properly and the chord distribution was doubled on purpose to increase the Reynolds numbers. This would make the turbine more comparable to larger wind turbines. *XFOIL* simulations showed that the *NREL S835* should be more suitable compared to the *DU91 W2-250* and the *FFA W2-211* aerofoils for this size of turbine. However, *XFOIL* uses simplified *NSE* to compute the pressure difference over an aerofoil. This limits the accuracy of the computed lift. Though it is known that the *NREL S835* aerofoil is designed for small scale turbines of 1-3 [m] diameter, whilst the *DU91 W2-250* and *FFA W2-211* aerofoils are not.

Section 2.2 discusses the design process of the TE flap and the driving mechanism. A bendable flap is designed, using the *Euler-Bernoulli* beam theory, that is able to make a gradual curvature over the chord-wise length of the flap. This design is preferred to a rotating rigid flap, as a sharp bend could lead to flow detachment. The results of the finite element simulation show that under load the flap indeed creates a gradual curvature and the stresses are well below the ultimate tensile stress of TPU.

Chapter 3 presents the results of this research. The results from the wind tunnel experiments in Section 3.1 show that the oscillating flaps work as intended. The flaps are able to change the camber, and with it the AOA, of the blade. The measured data show that the rotational speed and power increase with a deflected flap. However, the generator design choice, which was made several reports prior to this research, impacted the reliability of the results. The generator was too underpowered for the aerodynamic power generated by the rotor. This made the rotor speed up and resulted in low angles of attack. As a consequence, these results cannot confirm or disprove the theory on dynamic stall. However, a fix to the design is to install a heavier generator that is more in line with the aerodynamic power. Moreover, the reliability of the measured data is impacted by the wind tunnel and the measuring devices. The frequency of the generator and the measured wind speed in the tunnel could not be logged. The reliability of the results is hence influenced by human error.

Another set of measurements performed using a heavier generator in addition to a speed controller showed that the rotational speed of the turbine can be controlled very precisely. This improved setup is hence able to precisely control the AOA at the flap by actively setting the RPM of the turbine. However, a well defined conclusion on the influence of the oscillation frequency on dynamic stall could not yet be drawn. This was due to lack of time left in the wind tunnel to do enough experiments.

Section 3.2 discusses the results of the CFD analyses. The findings indicate that the length of the flap indeed has an influence on the performance of the blade. It also shows that a higher frequency and a larger amplitude both increase the lift coefficient. However, the reliability of the absolute values of the results is limited, as the used turbulence model is not the most accurate for dynamic simulations. The accuracy of the results could be improved by the use of a more suitable turbulence model like the LES. But this requires 3D simulations, which is beyond the scope of this project.

Future research could focus more on CFD simulations. A range of well known, commonly used aerofoils could be simulated to see which family of aerofoils would benefit most of the dynamic stall behaviour. A handful of profiles have already been simulated in the past with varying results. But a larger range of aerofoils could create classes of good and bad aerofoil types. This could be very interesting for companies that want to integrate the *Albatrozz* flaps in their blade designs.

Considering the experimental part of the research, the blade twist angle could be adjusted to allow for higher angles of attack at higher TSR. This will bring the peak power coefficient closer to the optimum TSR of 7 to 8 for three bladed turbines. Moreover, a lot of friction within the system can be reduced by

changing the tail rotor setup. Currently, the tail rotor is held in place by a linear bearing. This allowed for movement in axial direction and compressing of the spring coupling. Adding a flange to the axle and locking the flange in between two axial bearings should counteract this degree of freedom. In addition, a lot a friction is created by the wobbling of the nosecone. By extending the axle of the tail rotor, the nosecone can be directly mounted on the axle which should remove a lot a movement. Lastly, in the current setup the whole rotor assembly is held up by a 6 [mm] axle supported by one linear bearing. Freedom of movement can be reduced by increasing the diameter of the axle or by adding a second supporting bearing.

Another hypothesis that could be researched is the influence of the *Albatrozz* flaps on the negative effects of dynamic stall due to gusts. Currently, wind turbine blades are designed such that the AOA is somewhat below the peak lift coefficient. This is done to prevent gusts of wind to drag the blade into stall. It would be interesting to see what the response of a blade with *Albatrozz* flaps would be on the introduction of a sudden gust. This could be tested in a flow tank with pulses of fast increasing flow to simulate a gust.

5 Conclusion

The goal of this project was to design and test a one meter diameter scale wind turbine with *Albatrozz* flaps. This thesis builds upon previous research done within the bio-mimetic research group. In addition to the design of the flap, changes to the drive train design had to be made as well. Moreover, CFD simulations were performed to analyse the influence of the chord-wise length of the flap on the overall lift performance.

From the blade design study of Section 2.1 it is concluded that the chord and twist distribution had been accurately designed for the parameters of this turbine. However, two out of three aerofoils, the *DU91 W2-250* and the *FFA W2-211* aerofoils, were replaced with the *NREL S835* aerofoil as the latter should be more suitable for turbines of this scale.

The finite element analysis done on the designed flap in Section 2.2 concludes that the flap is able to make a gradual curvature, as opposed to a kink at the point of rotation. Moreover, the stresses in the flap go up to a maximum of about 0.63 [MPa], which is well below the ultimate tensile stress of 67 [MPa] for 3D printed TPU. The driving axle that is not rigidly connected to the TE also ensures that a gradual curvature, rather than a kink, is possible.

Section 2.3 assesses the safety of the rotor assembly. All connection and possible failure points between the blades and the nosecone are evaluated. The results conclude that the design is safe with a safety factor of at least ten. Which is sufficient but necessary considering that some parts are made using 3D printing.

The results of the CFD analyses show that the length of the flap as well as the frequency and amplitude of the oscillation do have an influence on the generated lift and drag. Where the shorter flap generates more lift for the same frequency and amplitude. Previous work done by the research group has already shown that a higher frequency and amplitude directly increase the lift performance. However, the CFD analyses of this thesis could not provide concrete evidence on the exact change in lift and drag values as the model could not yet accurately model the hysteresis curves.

The wind tunnel experiments showed that the designed *Albatrozz* flaps were able to oscillate at varying frequencies and that the oscillating flaps did indeed change the airflow. This could be concluded, as a change in flap deflection resulting in a change in rotational speed and measured power. Moreover, by replacing the weak generator by a more suitable one connected to a speed controller, the test setup was able to sweep through a set of TSR for any given wind speed. In addition, the speed controller board was able to accurately measure the power output and rotational speed of the generator. However, due to a lack of time and a lot of friction within the system the experiments could not yet show the dynamic stall behaviour.

The main recommendations that should be taken from this thesis is to improve upon the CFD model as well as on the experimental setup. The CFD model can be improved by switching from 2D to 3D analyses to allow for 3D effects to influence the lift behaviour. Moreover, a 3D model would allow for the implementation of LES rather than the SST RANS turbulence model. This could improve the dynamic stall behaviour within the CFD model. The experimental setup can be improved by changing the blade twist distribution, such that higher AOA is achieved at higher TSR. In addition, a lot of friction within the system can be reduced by adjusting the mounting of the tail rotor. The axial freedom of movement, for example, should be reduced such that the spring coupling is no longer compressed during the oscillation cycle. The wobbling of the nosecone should also be fixed by rigidly fixing the nosecone the the tail rotor axle. Moreover, it would be interesting to see the influence of high frequency oscillating flaps stall induced by gusts of wind. This could be tested in a flow tank by inducing steps of faster fluid flow whilst oscillating the aerofoil.

Bibliography

Airfoil Tools (2023). Naca 64(3)-418 (naca643418-il).

Batchelor, C. K. and Batchelor, G. K. (1967). *An introduction to fluid dynamics*. Cambridge university press.

Bauer, F. (2021). Tech-deep-dive: How kitekraft solves aerodynamics.

Beil, H. (2016). Biologisch inspirierte pitchbewegung des blattes einer windenergieanlage. Master's thesis, University of Groningen.

Bird Guides (2022). https://www.birdguides.com/cdn/gallery/birdguides/858a4695-387c-48f6-a7eb-6e824a28eae4.jpg.

Boorsma, K. and Schepers, J. (2014). New mexico experiment. *Preliminary Overview with Initial Validation Technical Report ECN-E–14-048 ECN*.

Budinski, K. G. (2014). *Materiaalkunde*. Pearson Education.

Carr, L. W. (1988). Progress in analysis and prediction of dynamic stall. *Journal of aircraft*, 25(1):6–17.

Carr, L. W., McAlister, K. W., and McCroskey, W. J. (1977). Analysis of the development of dynamic stall based on oscillating airfoil experiments. Technical report, NASA.

Choudhry, A., Arjomandi, M., and Kelso, R. (2016). Methods to control dynamic stall for wind turbine applications. *Renewable energy*, 86:26–37.

Comsol (2019a). The k- turbulence model.

Comsol (2019b). The sst turbulence model.

Comsol (2023). Understanding the fully coupled vs. segregated approach and direct vs. iterative linear solvers.

Comsol Multiphysics 6.0 (2021). Flow around an inclined naca 0012 airfoil. Technical report.

Corke, T. C. and Thomas, F. O. (2015). Dynamic stall in pitching airfoils: aerodynamic damping and compressibility effects. *Annual Review of Fluid Mechanics*, 47:479–505.

Cousteix, J. (2003). Aircraft aerodynamic boundary layers. In Meyers, R. A., editor, *Encyclopedia of Physical Science and Technology (Third Edition)*, pages 301–317. Academic Press, New York, third edition edition.

Frei, W. (2017). Which turbulence model should i choose for my cfd application?

Ge, M., Fang, L., and Tian, D. (2015). Influence of reynolds number on multi-objective aerodynamic design of a wind turbine blade. *PloS one*, 10(11):e0141848.

Gudmundsson, S. (2014). Chapter 8 - the anatomy of the airfoil. In Gudmundsson, S., editor, *General Aviation Aircraft Design*, pages 235–297. Butterworth-Heinemann, Boston.

IPCC (2023). Climate change 2023: Synthesis report. a report of the intergovernmental panel on climate change. contribution of working groups i, ii and iii to the sixth assessment report of the intergovernmental panel on climate change [core writing team, h. lee and j. romero (eds.)].

Janssen, F. (2018). New wind turbine based on lift enhancement due to oscillation. Master's thesis, University of Groningen.

KNMI (2022). Weerstations : Uurwaarnemingen. https://daggegevens.knmi.nl/klimatologie/uurgegevens. Assessed : 22-11-2022.

Lyu, P. (2016). Simulating turbulent flow in comsol multiphysics.

Madsen, H. A., Barlas, A., and Andersen, T. L. (2015). A morphing trailing edge flap system for wind turbine blades. In *Proceedings of the 7th ECCOMAS thematic conference on smart structures and materials (SMART 2015)*, volume 7. IDMEC.

Mahfoozi, S. (2020). A biomimetic approach in design and construction of a wind turbine utilizing unsteady aerodynamics for enhanced lift. Master's thesis, University of Groningen.

Manwell, J., McGowan, J., and Rogers, A. (2010a). Wind energy explained: theory, design and application.

Manwell, J., McGowan, J., and Rogers, A. (2010b). *Wind Energy Explained: Theory, Design and Application*. Wiley, 2 edition.

Marchant, A. (2017). Investigation of a wind turbine blade model adapted from the albatross landing technique , at increased scale. Master's thesis, University of Groningen.

Matz, D. (2010). Lift enhancement on aerofooils via oscillating angles of attack after the example of an albatross - a numerical study. Master's thesis, University of Groningen.

McAlister, K. W., Carr, L. W., and McCroskey, W. J. (1978). Dynamic stall experiments on the naca 0012 airfoil. Technical report.

McCroskey, W. J. (1981). The phenomenon of dynamic stall. Technical report.

McIntosh, S. C. (2009). *Wind energy for the built environment*. PhD thesis, University of Cambridge.

Muhsen, H., Al-Kouz, W., and Khan, W. (2019). Small wind turbine blade design and optimization. *Symmetry*, 12(1):18.

Mulleners, K. and Raffel, M. (2013). Dynamic stall development. *Experiments in fluids*, 54:1–9.

Neven, E. (2020). Biomimetic optimization of wind turbines using unsteady aerodynamics. Master's thesis, University of Groningen.

Neven, E. and Stamhuis, E. (2019). Biomimetic optimization of wind turbines at low wind speeds using unsteady aerodynamics. Technical report, University of Groningen.

Noffke, N. (2011). Investigation on the unsteady aerodynamics of the landing behaviour of the petrel fulmarus glacialis and discussion on application potential. Master's thesis, University of Groningen.

Reddy, J. (2008). *Nonlinear Finite Element Analysis*. Oxford University Press.

Rüppell, G. (1977). The course of the upper-side flow on a wing model of the fulmar (fulmarus glacialis) in slow flight. *Fortschritte der Zoologie*, 24:287–295.

Schepers, J., Boorsma, K., Cho, T., Gomez-Iradi, S., Schaffarczyk, P., Shen, W., Lutz, T., Stoevesandt, B., Schreck, S., Micallef, D., et al. (2012). Analysis of mexico wind tunnel measurements. final report of iea task 29, mexnext (phase 1). *ECN*.

Schepers, J., Lutz, T., Boorsma, K., Gomez-Iradi, S., Herraez, I., Oggiano, L., Rahimi, H., Schaffarczyk, P., Pirrung, G., Madsen, H. A., et al. (2018). Final report of iea wind task 29 mexnext (phase 3). *ECN*.

Schubel, P. J. and Crossley, R. J. (2012). Wind turbine blade design. *Energies*, 5(9):3425–3449.

Schweickert, F. (2016). Design investigate a biomimetic adaption for a wind turbine blade applying unsteady aerodynamics. Master's thesis, University of Groningen.

Stamhuis, E., van Ek, G., and de Lange, E. (2019). Project plan albatrozz. Technical report.

Ultimaker (2022). Ultimaker tough pla technical data sheet.

Vogel, S. and Savage, A. (1996). Life in moving fluids. the physical biology of flow. *Biological Journal of the Linnean Society*, 57(3):291.

Wallpapergeeks (2014). https://www.wallpapergeeks.com/wp-content/uploads/2014/03/Gibsons-Wandering-Albatross-New-Zealand.jpg.

Warham, J. (1991). The petrels: their ecology and breeding systems. *The Academic Press*.

Zaaijer, M. and Viré, A. (2021). Introduction to wind turbines: Physics and technology. Lecture notes, TU Delft.

Zhang, Y., Van Zuijlen, A., and Van Bussel, G. (2014). Comparison of cfd simulations to non-rotating mexico blades experiment in the ltt wind tunnel of tu delft. In *Journal of Physics: Conference Series*, volume 524, page 012013. IOP Publishing.

A Stakeholders and their roles

The list of stakeholders for this project consists of a few priority and a few additional stakeholders. The priority stakeholders have a more direct relation to the project compared to the additional stakeholders and are hence more influential. Table A.1 and A.2 show the priority and additional stakeholders respectively.

Eize J. Stamhuis is a professor at the university of Groningen and the founder of the Albatrozz technology. He will be the main supervisor of this project.
Clemens Verhoosel is an associate professor in the section of *'Energy Technology'* at the technical university of Eindhoven. Clemens will be the responsible supervisor from the TU Eindhoven.

Table A.1: Priority stakeholders

Name	**Title**	**Role**
Eize J. Stamhuis	Associate professor at the university of Groningen and founder of the Albatrozz project	Project supervisor
Clemens Verhoosel	Associate professor at TU Eindhoven	Home university supervisor

There are also a number of additional stakeholders for this project. To start with the initiators of Albatrozz B.V. The initiators consist of RG-projecten B.V., EmpowerMi and previously mentioned professor Stamhuis. These initiators are the shareholders of the umbrella company Albatrozz B.V. However, except for professor Stamhuis they are not directly involved into this project.
Another additional stakeholder is dr. Peter Boelen who is the technical staff at the university of Groningen. He can advice and assist with the technical design of the Albatrozz flaps on the scale model wind turbine.
University of Groningen is the host university who will provide the necessary equipment like a study desk and the wind tunnel.
Furthermore the wind energy industry is an important additional stakeholder, not for the course of the project but definitely for the end result. The industry has to implement the Albatrozz technology into existing and future wind turbine models.
The final stakeholder is the governmental institution that approves the concept on safety. Again this stakeholder is not very important for this specific research, but it is important for the implementation of the technology on a larger scale.

Table A.2: Additional stakeholders

	Function	**Role**
RG-projecten B.V.	2^{nd} initiator of the Albatrozz project	Project management and advisor of Albatrozz, no real role in this project
EmpowerMi	3^{rd} initiator of the Albatrozz project	Consultancy of Albatrozz, no real role in this project
Peter Boelen	Technical staff	Advices on technical aspects of the design and experimental setup
University of Groningen	Host university	Provides study desk, study facilities, mechanical workshop and wind tunnel
Industry	Client	Implements the Albatrozz technology into larger wind turbines, no real role in this project
Government	Institution for safety	Approves safety of concept